# Factors controlling the bifurcation structure of sea ice retreat

Ian Eisenman[1,2]

Received 27 April 2011; revised 25 October 2011; accepted 28 October 2011; published 14 January 2012.

[1] The contrast in surface albedo between sea ice and open ocean suggests the possibility of an unstable climate state flanked by two separate stable climate states. Previous studies using idealized single-column models and comprehensive climate models have considered the possibility of abrupt thresholds during sea ice retreat associated with such multiple states, and they have produced a wide range of results. When the climate is warmed such that the summer minimum Arctic sea ice cover reaches zero, some models smoothly transition to seasonally ice-free conditions, others discontinuously transition to seasonally ice-free conditions, and others discontinuously transition to annually ice-free conditions. Among the models that simulate a continuous transition to seasonally ice-free conditions, further warming causes some to smoothly lose the remaining wintertime-only sea ice cover and others to discontinuously lose it. Here, we use a toy model representing the essential physics of thermodynamic sea ice in a single column to investigate the factors controlling which of these scenarios occurs. All of the scenarios are shown to be possible in the toy model when the parameters are varied, and physical mechanisms giving rise to each scenario are investigated. We find that parameter shifts that make ice thicker or open ocean warmer under a given climate forcing make models less prone to stable seasonally ice-free conditions and more prone to bistability and hence bifurcations. The results are used to interpret differences in simulated sea ice stability in comprehensive climate models.

**Citation:** Eisenman, I. (2012), Factors controlling the bifurcation structure of sea ice retreat, *J. Geophys. Res.*, *117*, D01111, doi:10.1029/2011JD016164.

## 1. Introduction

[2] When the polar sea ice cover recedes, the change in surface albedo causes an increase in absorbed solar radiation, which promotes further warming and hence more sea ice loss. The idea that this positive feedback may lead to instability has a long history in climate science. Early diffusive energy balance models of the annual-mean global climate system [*Budyko*, 1969; *Sellers*, 1969] often exhibit multiple states due to this feedback. For some values of the solar constant in a typical energy balance model, five different solutions are possible: depending on the initial condition, the model can settle on (i) a stable completely ice-covered state, (ii) an unstable state with ice edge in low latitudes, (iii) a stable state with ice edge in midlatitudes, (iv) an unstable state with ice edge in polar latitudes, and (v) a stable completely ice-free state (see review by *North* [1990]). However, these states exist only in a limited region of the parameter space. Only ice-free solutions are possible when the solar constant is large, and only ice-covered solutions are possible when the solar constant is small. Hence when the climate is warmed in such a model from modern-like conditions, the ice edge gradually recedes poleward to about 70 degrees latitude, and then a bifurcation point is crossed and the entire remaining ice cover abruptly disappears. This abrupt loss of ice is irreversible in the sense that the climate must be cooled considerably beyond the initial transition point for the ice cover to return, and the ice edge traces out a hysteresis loop as the solar constant is varied. The irreversibility is associated with the existence of two stable states separated by an unstable state in a finite region of the parameter space.

[3] The observed loss of Arctic sea ice during recent decades has prompted increased interest in the question whether sea ice retreat in the real world exhibits bifurcation thresholds similar to diffusive energy balance models, i.e., whether the retreating Arctic sea ice cover will pass a tipping point [*Eisenman and Wettlaufer*, 2009, and references therein]. If a tipping point is defined as an irreversible jump in the sea ice cover as the forcing is gradually varied, then an unstable sea ice state is a necessary condition for a tipping point to be possible in a simple dynamic system.

[4] Recent studies examining the possibility of bifurcation thresholds during sea ice retreat have produced a range of results which are summarized in Figure 1. Starting from modern conditions with sea ice cover throughout the year (blue shading in Figure 1), warming can cause the Arctic Ocean to become seasonally ice-free (red shading), and then, under extreme warming, to become ice-free throughout the year (gray shading). As described below, some studies have

[1]Geological and Planetary Sciences, California Institute of Technology, Pasadena, California, USA.
[2]Atmospheric Sciences, University of Washington, Seattle, Washington, USA.


0148-0227/12/2011JD016164

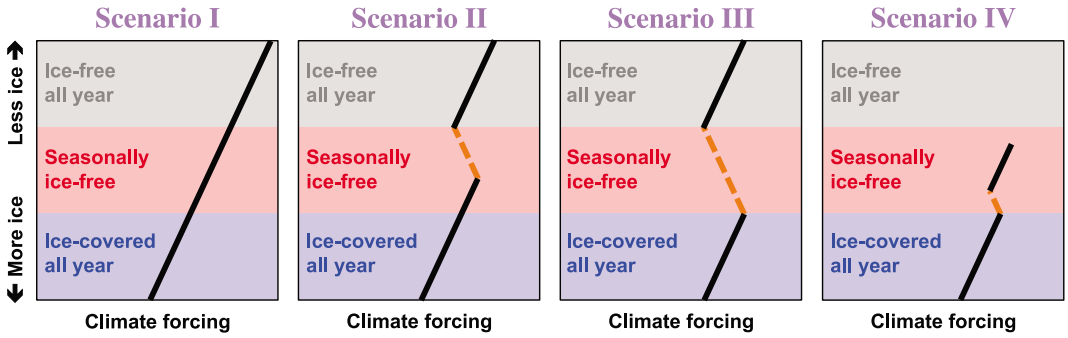


**Figure 1.** Sketch of the range of results from previous studies using single-column models and GCMs. Solid black lines indicate stable states and orange dashed lines indicate unstable states. Bifurcation thresholds occur where solid and dashed lines intersect. Note that annually ice-free conditions are not included in Scenario IV as this is meant to describe studies that typically do not discuss further warming after the loss of the summer ice cover.

suggested that the complete loss of the current Arctic sea ice cover would occur in a continuous and reversible fashion (Scenario I in Figure 1), others have suggested that the loss of summer sea ice is reversible but a discontinuity would occur during the final loss of a wintertime-only sea ice cover (Scenario II), others have suggested that warming beyond perennial ice conditions would cause a large jump to completely ice-free conditions with no stable seasonal ice cover being possible (Scenario III), and others have suggested that there would be a jump during the transition to stable seasonally ice-free conditions (Scenario IV).

[5] A recent evaluation of threshold behavior during anthropogenic climate change identified the loss of the summertime sea ice cover in the Arctic as a threshold (Scenario IV), finding it to be the most imminent tipping point in the global climate system [*Lenton et al.*, 2008]. This finding was based on an aggregation of the opinions of experts at a workshop, an elicitation of the opinions of other experts, and a review of the literature.

[6] Several recent studies have investigated aspects of the possibility of bifurcation thresholds in comprehensive coupled atmosphere-ocean global climate models (GCMs). *Holland et al.* [2006] found that some GCMs exhibit abrupt reductions in summer minimum Arctic sea ice cover during 21st century climate projections, with large reduction events in some simulations causing an early onset of seasonally ice-free conditions. These results elevated the widespread concern that the summer minimum sea ice cover might pass a tipping point [e.g., *Serreze*, 2011], which would be Scenario IV. However, further analysis of the simulations revealed that abrupt increases in summer ice extent occur just as frequently as abrupt decreases, with the year-to-year variability about the long-term decline increasing as the ice cover diminishes but no significant skewness in the anomalies [*Holland et al.*, 2008]. This implies a noisy but continuous loss of the summer sea ice cover, consistent with Scenario I or II. *Winton* [2008] also examined GCM simulations of 21st century climate, and he found linear relationships between polar albedos, polar temperatures, and global temperatures, supporting Scenario I or II. *Winton* [2006, 2008] further examined two GCMs which produced annually ice-free Arctic Ocean conditions in response to extreme greenhouse forcing. In both GCMs, the linear relationships were not affected when the Arctic Ocean transitioned to seasonally ice-free conditions. However, after global temperatures further warmed by several degrees, one of the GCMs began to show a sharp increase in the surface albedo feedback, exhibiting heat budget changes consistent with the presence of an unstable state in diffusive energy balance models. This drove an abrupt elimination of the remaining wintertime-only sea ice cover in the GCM (Scenario II). The other GCM exhibited an approximately linear transition to annually ice-free conditions (Scenario I). *Ridley et al.* [2008] found that a different GCM also exhibited nonlinear behavior. Arctic sea ice cover initially declined linearly with global temperature in this model, but the final loss of the winter sea ice cover was abrupt and nonlinear in global temperature. Further evidence such as cycles of collapse and recovery of the winter sea ice cover under steady forcing was used to argue for the existence of two stable winter sea ice cover states in this model under extreme warming (Scenario II). Some studies have also manually removed sea ice in GCMs and examined whether it recovers. *Winton* [2008] did not allow sea ice to form in two versions of the Geophysical Fluid Dynamics Laboratory GCM. He found that although the surface absorbed more solar radiation due to the change in albedo, this was more than compensated by an increase in longwave radiation and turbulent heat loss due to the change in surface temperature, implying that the ice would grow back and hence that there is no unstable state under modern forcing in this GCM with less sea ice than the simulated modern sea ice cover. *Schroeder and Connolley* [2007] found that sea ice recovered within a few years when it was manually removed in a GCM simulation with preindustrial forcing. Similarly, *Tietsche et al.* [2011] found that when they removed all of the Arctic sea ice at various times during a simulation of 21st century climate with a different GCM, the ice extent recovered within about 2 years. These three manual ice removal studies all suggest the lack of an imminent unstable sea ice state and hence support Scenario I or II. *Armour et al.* [2011] directly addressed the possibility of irreversibility during sea ice retreat in a GCM by increasing $CO_2$ until the simulated Arctic Ocean became entirely ice-free throughout the year and then decreasing $CO_2$ until all the ice returned. The results showed no evidence for multiple states outside

the envelope of year-to-year variability, indicating that the GCM used in that study supports Scenario I. Finally, *Ferreira et al.* [2011] found that a GCM with intermediate complexity atmospheric physics and two different idealized geographic configurations was capable of simulating both a nearly ice-free climate and a climate with perennial ice extending to midlatitudes under the same forcing, thereby implying a region of instability consistent with Scenarios II-IV without distinguishing between the scenarios. Taken together, these results imply that some comprehensive GCMs simulate Scenario I and others simulate Scenario II, with only a few of studies simulating sufficiently large warming to distinguish between the scenarios.

[7] "Toy" models, i.e., conceptual mathematical models, are computationally cheap and can provide a level of mechanistic understanding that is often not feasible with GCMs. Recent toy models of sea ice and climate have typically employed a single-column representation. In a simple conceptual representation of the influence of a temperature-dependent surface albedo on an annual-mean single-column picture of earth's climate, an unstable state analogous to the unstable solutions of diffusive energy balance models exists for some parameter choices [*North*, 1990]. Adding a fundamental representation of seasonally varying sea ice thickness to this picture, *Thorndike* [1992] modeled seasonal thermodynamic sea ice growth and ablation in an ocean mixed layer below a linear energy balance atmospheric column. The intriguing result of this study is that all seasonally ice-free solutions are unstable. When the forcing in this model is gradually increased, the model abruptly transitions from annually ice-covered to annually ice-free conditions (Scenario III). Similarly, *Muller-Stoffels and Wackerbauer* [2011] found bistability between annually ice-covered and annually ice-free states with no stable seasonal ice cover (Scenario III) in a horizontally homogeneous layer of ice-ocean cells with specified atmospheric and oceanic forcing at the vertical boundaries. In contrast to this, a recent single-column model allowed stable seasonally ice-free solutions [*Eisenman and Wettlaufer*, 2009]: a gradual increase in forcing lead to a smooth transition from perennial sea ice to seasonally ice-free conditions, but at some point as the forcing continued to increase the remaining wintertime-only sea ice cover abruptly disappeared (Scenario II). Results consistent with Scenario II were also found using a variant of this model that included a representation of fractional sea ice area and other additional physical processes [*Eisenman*, 2007]. Similarly, an intermediate-complexity single-column model with prognostic vertical structure of ocean temperature and salinity and 40 different sea ice thickness categories simulated results consistent with Scenario II [*Björk and Söderkvist*, 2002]. However, a variant of the *Eisenman and Wettlaufer* [2009] model with a parameterized representation of clouds simulated a bifurcation at the point of transition to seasonally ice-free conditions for some choices of the cloud feedback parameters [*Abbot et al.*, 2011], supporting Scenario IV. *Merryfield et al.* [2008] similarly found results supporting Scenario IV in an idealized mathematical representation of the processes governing the *Holland et al.* [2006] GCM behavior. Finally, *Flato and Brown* [1996] used a single-column model with a sensitive parameterization of the dependence of surface albedo on temperature, ice thickness, and snow thickness, and they found that seasonal and perennial ice states were both possible under the same forcing, consistent with Scenario IV. Hence Scenarios II, III, and IV have all occurred in different single-column models in previous studies.

[8] In summary, each of the four contrasting scenarios illustrated in Figure 1 has been supported by multiple models in previous studies, which raises the question what physical factors determine which scenario occurs and hence which scenario is most likely in the real world. We address this question by exploring the range of possibilities in a stripped down toy model representing the essential physics of sea ice in a single column. The parameters are varied broadly, which is meant to provide an analogy to adding representations of additional physical processes. We find that the toy model is able to reproduce the full range of previous single-column model and GCM results (Scenarios I-IV), depending on the parameter values. This toy model is sufficiently simple that its behavior can be rigorously understood, and we examine the physical mechanisms that give rise to the toy model behavior and parameter dependencies. The analysis is used to build a conceptual framework for understanding other model results and thereby assessing their relevance to the real world.

## 2. Idealized Sea Ice Model

[9] The model used in this study represents a slab of ice floating in a uniform ocean mixed layer below a time-varying linear atmosphere. It is meant to represent the skeleton of sea ice variability in single-column models and GCMs, i.e., the essential physics governing the thermodynamic evolution of sea ice in a single column and nothing else. The intent is thus that the results of this model will be qualitatively robust across the range of single-column sea ice models discussed above and informative for understanding sea ice results from GCMs.

[10] Thermodynamic changes in sea ice thickness are primarily controlled by vertical diffusion within the ice, a Stefan condition for growth or ablation at the ice-ocean interface, and a Stefan condition for ablation at the upper surface when the temperature warms to the melting point. The influence of snow on the ice surface and bulk salinity within the ice also play a role, but for simplicity they are not explicitly included here. Solving the equations for these processes under observationally based forcing produces a seasonal cycle in sea ice thickness and temperature that is consistent with observations [*Maykut and Untersteiner*, 1971]. *Semtner* [1976] developed a numerical scheme to efficiently include these processes in gridded models, and the thermodynamic component of the sea ice representation in most current GCMs is based on this scheme.

[11] The toy model we use in this study is a simplified variant of the model developed by *Eisenman and Wettlaufer* [2009] (hereafter EW09). A derivation starting from the model of EW09 is provided in section 2.1. This toy model is approximately equivalent to the model of *Semtner* [1976] with no prognostic temperature levels ("zero-layer model") and with the addition of simple representations of the ocean mixed layer and atmosphere. It is also approximately equivalent to the model of *Thorndike* [1992] with a smoothed seasonal cycle in forcing and zero specific heat capacity of sea ice. These similarities strengthen the case that the toy

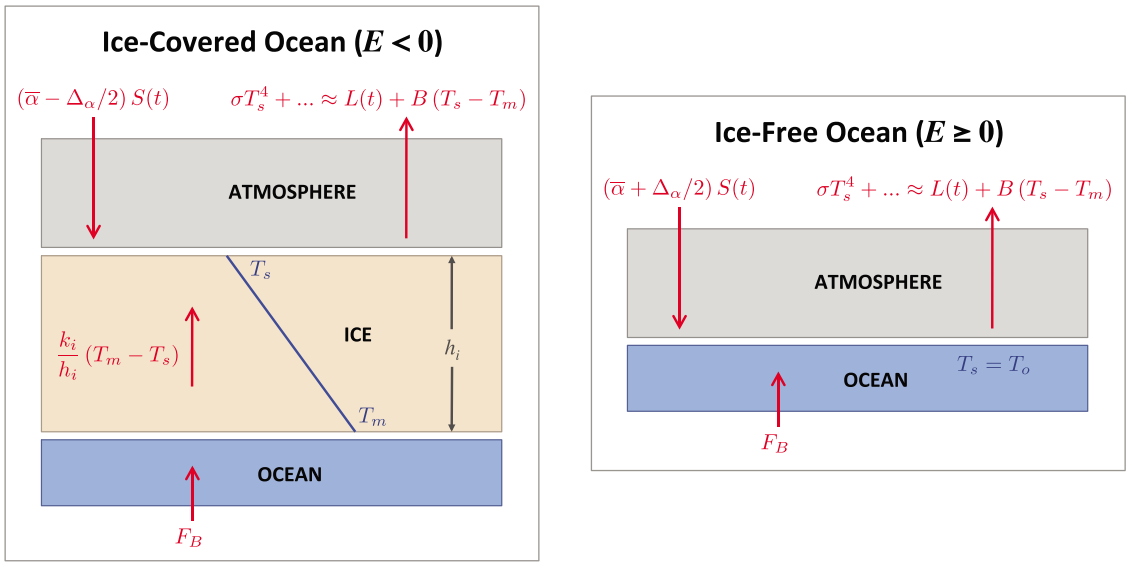


**Figure 2.** Schematic illustrating the toy model employed in this study, which is a single-column representation of the atmosphere, sea ice, and ocean mixed layer. Red arrows indicate energy fluxes, with $S(t) \equiv S_m - S_a\cos 2\pi t/P$ being solar forcing and $L(t) + B(T_s - T_m) \equiv L_m + L_a\cos 2\pi(t/P - \phi) + B(T_s - T_m)$ representing the sum of a linearized approximation of upwelling thermal radiation ($\sigma T_s^4$), downwelling thermal radiation, and turbulent surface fluxes. A linear temperature profile is assumed within the sea ice (blue line).

model results presented here are relevant for understanding the physical mechanisms causing the range of previous toy model and GCM results illustrated in Figure 1.

[12] The toy model is illustrated schematically in Figure 2. It evolves a single variable representing the surface enthalpy ($E$), which varies smoothly between ice-covered and ice-free model states, as in the model of EW09. When ice is present, the ocean mixed layer temperature ($T_o$) is fixed at the melting point ($T_m$) and the ice thickness ($h_i$) evolves, and when ice is absent the ocean mixed layer temperature evolves. The surface enthalpy describes how far the system is, in terms of energy per unit surface area, from the transition point between ice-covered and ice-free conditions:

$$E \equiv \begin{cases} -L_i h_i & E < 0 \text{ [sea ice]} \\ c_o H_o (T_o - T_m) & E \geq 0 \text{ [ocean]} \end{cases} \tag{1}$$

with $L_i = 3 \times 10^8 \mathrm{Jm}^{-3}$ the sea ice latent heat of fusion and $c_o H_o = 2 \times 10^8 \mathrm{Jm}^{-2}\mathrm{K}^{-1}$ the heat capacity of the ocean mixed layer (using a 50 m depth). The surface enthalpy evolves according to

$$\frac{dE}{dt} = f(t, E) \tag{2}$$

with the net energy flux into the system being

$$f(t, E) = A - BT + F_B. \tag{3}$$

Here $T \equiv T_s - T_m$ is the departure of the surface temperature ($T_s$) from the melting point, $A - BT$ represents a linearization of the dependence of the net surface flux on the surface temperature, and $F_B$ is the heat flux into the bottom of the sea ice or ocean mixed layer. We treat $B$ and $F_B$ as constants, and formulae for $A$ and $T$ are given below.

[13] The surface flux ($A - BT$) can be viewed as comprising only net shortwave (i.e., solar) and longwave (i.e., thermal) radiation, although the default parameter values will be chosen to additionally account for turbulent surface fluxes of sensible and latent heat (see section 2.1). The temperature-independent component of the surface net longwave flux varies seasonally due to atmospheric energy flux convergence and the seasonal cycle in optical depth (see section 2.1). We approximate both longwave and shortwave seasonal variations to be sinusoidal with a specified phase offset ($\phi$) between them:

$$A = \left(\bar{\alpha} + \frac{\Delta_\alpha}{2}\tanh\frac{E}{L_i h_\alpha}\right)\left(S_m - S_a\cos 2\pi\frac{t}{P}\right) - \left[L_m + L_a\cos 2\pi\left(\frac{t}{P} - \frac{\phi}{P}\right)\right]. \tag{4}$$

Here $\bar{\alpha}$ and $\Delta_\alpha$ are the mean and difference, respectively, in coalbedo between ice and ocean (with coalbedo $\equiv 1 -$ albedo), $h_\alpha$ is a parameter dictating the smoothness of the albedo transition as $E$ passes through zero, $S_m$ and $S_a$ describe the shortwave forcing, $L_m$ and $L_a$ describe the longwave (and turbulent) forcing, $P = 1$ year is the period of the forcing, and time is referenced to the winter solstice (i.e., minimum shortwave forcing occurs at $t = 0$).

[14] There are three possible regimes for the surface temperature, which are separated by thresholds associated with solid–liquid phase transitions. (i) If no ice is present, the surface temperature is equal to the ocean mixed layer temperature ($T_s = T_o$). (ii) If ice is present but surface melt is occurring, the surface is at the melting point ($T_s = T_m$). We assume that the energy required to heat or cool the ice is negligible (see section 2.3), and hence surface melt occurs whenever there is flux into the surface ($A - BT = A > 0$). (iii)

**Table 1.** Dimensionless Variables and Parameters

| Symbol | Definition | Description | Value |
|---|---|---|---|
| | | *Variables* | |
| $\tilde{t}$ | $t/P$ | Time | $t$/1yr |
| $\tilde{E}$ | $E/(\overline{\alpha}S_m P)$ | Surface enthalpy | $T$/8.8K or $-h_i$/5.9m |
| $\tilde{T}$ | $T/\left(\frac{\overline{\alpha}S_m P}{c_o H_o}\right)$ | Surface temperature (diagnostic) | $T$/8.8K |
| | | *Parameters* | |
| $\tilde{S}_a$ | $S_a/S_m$ | Shortwave seasonal amplitude | 1.5 |
| $\tilde{L}_m$ | $L_m/(\overline{\alpha}S_m)$ | Longwave annual mean | 1.25 |
| $\tilde{L}_a$ | $L_a/(\overline{\alpha}S_m)$ | Longwave seasonal amplitude | 0.73 |
| $\tilde{\phi}$ | $\frac{\phi}{P}$ | Longwave seasonal time lag | 0.15 |
| $\tilde{B}$ | $B/\left(\frac{c_o H_o}{P}\right)$ | Longwave temperature dependence | 0.45 |
| $\tilde{\zeta}$ | $L\frac{k_i}{B}/(\overline{\alpha}S_m P)$ | Thermodynamic scale thickness | 0.12 |
| $\tilde{\Delta}_\alpha$ | $\Delta_\alpha/(2\overline{\alpha})$ | Surface albedo jump | 0.43 |
| $\tilde{h}_\alpha$ | $h_\alpha/\left(\frac{\overline{\alpha}S_m P}{L_i}\right)$ | Range of $\tilde{E}$ for albedo jump | 0.08 |
| $\tilde{F}_B$ | $F_B/(\overline{\alpha}S_m)$ | Heat flux into bottom of model domain | 0 |

If ice is present and the surface is not melting, no energy can accumulate at the surface, and the surface temperature is calculated from a balance of fluxes at the ice-atmosphere interface. In this scenario, the surface temperature is colder than the melting point ($T_s < T_m$), whereas the temperature at the phase interface marking the base of the ice must be equal to the melting point ($T_{\text{base}} = T_m$), as illustrated in Figure 2 (left). We neglect salinity effects and treat the melting temperature as constant. With negligible sensible heat capacity in the ice, the temperature profile is always approximately linear (see section 2.3), and hence the diffusive heat flux upward through the ice is equal to $k_i(T_{\text{base}} - T_s)/h_i = -k_i T/h_i$, with $k_i$ being the thermal conductivity of ice. The temperature of the frozen ice surface is calculated by setting this flux equal to the flux between the surface and the atmosphere,

$$-\frac{k_i T}{h_i} = -A + BT, \tag{5}$$

and solving for $T$. The three regimes for the surface temperature are combined as

$$T = \begin{cases} \dfrac{E}{c_o H_o} & E \geq 0 \quad \text{[open ocean]} \\ 0 & E < 0,\ A > 0 \ \text{[sea ice, melting surface]} \\ \dfrac{A}{B}\left(1 + \dfrac{\zeta}{h_i}\right)^{-1} & E < 0,\ A < 0 \ \text{[sea ice, frozen surface]} \end{cases}, \tag{6}$$

where the constant

$$\zeta \equiv \frac{k_i}{B} \tag{7}$$

is introduced here as the thermodynamic scale thickness for sea ice and described in more detail in section 2.2. Inserting equation (1), $\zeta/h_i = -\zeta L_i/E$ in equation (6), and hence equations (2)–(4) and (6) fully specify the ordinary differential equation for the time evolution of $E$.

[15] The following sections further describe the toy model formulations. Readers less concerned with the model details may choose to skip forward to Table 1, where the dimensionless model quantities are listed, and then to section 3.

### 2.1. Derivation of Default Parameter Values

[16] Here we derive default parameter values for the toy model (equations (2)–(4) and (6)) to make it approximately equivalent to the model of EW09, which was derived from first principles in that study and demonstrated to generate an observationally consistent Arctic sea ice seasonal cycle. We also examine the influence of the simplifications employed in this toy model compared with EW09.

[17] Three terms in the EW09 surface flux depend on time: (i) shortwave forcing is specified from surface observations; (ii) the temperature-independent component of the surface net longwave and turbulent flux forcing is specified based on the seasonal cycle in atmospheric optical depth associated with water vapor and clouds, as well as the specified temperature equatorward of the model domain which influences atmospheric energy flux convergence; and (iii) the temperature dependence of the surface flux varies based on the seasonal cycle in optical depth. Each of these terms has been approximated as a sinusoid or constant in equations (2)–(4) and (6). For the first and second terms, we use the one-year sinusoidal component from a Fourier transform of the forcing used by EW09, and for the third term we use the annual-mean value from EW09. This leads to $S_m = 100$ Wm$^{-2}$, $S_a = 150$ Wm$^{-2}$, $L_m = 85$ Wm$^{-2}$, $L_a = 41$ Wm$^{-2}$, $\phi = 0.15$ years, and $B = 2.83$ Wm$^{-2}$/K. The longwave forcing term peaks $\phi = 0.15$ years after the summer solstice, when maritime surface temperatures are typically largest, both because of increased atmospheric optical depth allowing less longwave radiation to escape to space in late summer than in winter and because the temperature equatorward of the model domain in the representation of atmospheric energy flux convergence is largest in late summer. Note that under this approximation the solar forcing, which multiplies the surface albedo, becomes negative during part of the winter, unlike in the real world. This is, however, an accurate representation of the leading Fourier component of the observed solar forcing. Higher order harmonics modify the final result of EW09 such that the solar forcing is nonnegative throughout the year, but including only the dominant Fourier component does not substantially alter the model solution, as discussed below in this section (see also section 5.3 where the bifurcation structure of the toy model used here is compared with the EW09 model).

[18] The surface albedo occurs in two places in the system (2)–(4) and (6). First, it occurs in the net shortwave flux forcing the evolution of $E$ (part of $A$ in equation (3)). Second, it occurs in the ice surface temperature (part of $A$ in equation (6)). In the model of EW09, where the albedo occurs in two similar places in the model equation, the dependence of the albedo on $E$ was smoothed in the first occurrence to allow a gradual transition from ice-covered to ice-free net shortwave forcing. An equivalent treatment of the equation for the surface temperature would be to smooth the transition between the $E \geq 0$ and $E < 0$ regimes. This was expected to have a smaller impact on the results of EW09 because the unsmooothed temperature varies continuously as $E$ crosses through zero, and hence this additional smoothing was not employed by EW09 in the interest of keeping the equations as transparent as possible. Here for simplicity we use the same smoothed dependence of the surface albedo on $E$ in both instances where the albedo occurs in the model equations.

[19] The seasonal cycle of ice thickness and surface temperature in the EW09 model is plotted in Figure 3 (dark blue). The simplifications of the time-dependent forcing discussed above, as well as the adjustment of the albedo representation in the surface temperature, have only a small impact on the EW09 model solution (light blue). Winter temperatures decrease due to the negative solar forcing associated with using only the leading Fourier component, but the seasonal cycle in the model state ($h_i$) is not substantially affected.

[20] The EW09 model also includes a representation of ocean heat flux into the bottom of the sea ice or ocean mixed layer, as well as wind-driven ice export out of the model domain. Both of these terms are quantitatively important for the simulated seasonal cycle under a given forcing (green and orange curves in Figure 3), but setting them to zero in the toy model is not expected to influence the qualitative bifurcation structure when the parameters are varied (see section 5.3), and it makes the model more readily interpretable. Furthermore, the presence or absence of sea ice motion in the current suite of GCMs does not appear to be a dominant factor for the simulation of sea ice retreat compared with other differences among the models [*Eisenman et al.*, 2011]. We set ice export to zero in the toy model; we set $F_B = 0$ in the default parameter regime, but we retain the term in equations (2)–(4) and (6) and vary it in the sensitivity analysis.

[21] Removing ice export and basal heat flux both cause the simulated ice thickness to increase. In order to get an observationally reasonable Arctic sea ice seasonal cycle in the toy model, we compensate for these simplifications by reducing the annual-mean longwave radiative cooling to $L_m = 70$ Wm$^{-2}$. All other toy model parameters are set at default values identical to those of EW09: $\zeta \equiv k_i/B = 0.7$m, $\bar{\alpha} \equiv 1 - (\alpha_i + \alpha_o)/2 = 0.56$, $\Delta_\alpha \equiv \alpha_i - \alpha_o = 0.48$, and $h_\alpha = 0.5$m.

[22] With the changes described in this section, the EW09 model becomes equivalent to the system (2)–(4) and (6) (red curves in Figure 3).

### 2.2. Thermodynamic Scale Thickness

[23] The constant $\zeta$ is defined in equation (7) as the thermodynamic scale thickness for sea ice. This quantity describes the tendency for thin ice to grow considerably more rapidly than thick ice, thereby encapsulating the nonlinear thermodynamic effects of sea ice growth during winter.

[24] During winter, the surface flux balance (equation (5)) involves three terms: (i) diffusive heat flux upward through the ice that leads to congelation at the ice-ocean interface ($-k_iT/h_i > 0$), (ii) a forcing term that promotes cooling ($-A > 0$), and (iii) the temperature-dependent term in the surface flux ($BT < 0$). The quantity $h_i/\zeta$ describes the ratio between terms (iii) and (i). When $h_i \ll \zeta$, the dominant balance in equation (5) is between terms (i) and (ii). This leads to rapid ice growth: in this regime, equations (2)–(4) and (6) reduce to $L_i dh_i/dt \approx |A|$ during ice-covered winter. The dominant balance in equation (5) when $h_i \gg \zeta$ is between terms (iii) and (ii). Diffusive heat flux in the ice is negligible in this regime, and equations (2)–(4) and (6) give negligible ice growth ($L_i dh_i/dt \approx 0$).

[25] This discussion of the asymptotic $h_i \ll \zeta$ and $h_i \gg \zeta$ regimes brackets the nonlinear stabilizing effect of sea ice growth. Thin ice grows faster than thick ice, and this dependence gets steeper as ice thins.

### 2.3. Stefan Number

[26] In the derivation of equation (6), we assumed that sensible heat changes were negligible and equivalently that the temperature profile could be approximated as linear. The Stefan number describes the ratio of latent heat changes to sensible heat changes, and this was a large Stefan number approximation. Here we derive the thickness range for which this approximation is valid.

[27] We consider a diffusion equation for temperature ($c_i \partial T/\partial t = k_i \partial^2 T/\partial z^2$) within ice of thickness $h_i$ subject to a specified flux ($f$) out of the surface boundary and a Stefan condition for thickness change at the lower boundary ($-k_i \partial T/\partial z = L_i dh_i/dt$). Here $c_i = 2 \times 10^6$ J/m$^3$/K is the volumetric heat capacity of ice. Integrating the diffusion equation from the base of the ice to the surface leads to the following equation:

$$f = L_i \frac{dh_i}{dt} - c_i h_i \frac{d\bar{T}}{dt} \tag{8}$$

with $\bar{T} \equiv (1/h_i)(\int_{-h_i}^{0} T dz)$ the column-averaged temperature. The ratio between the two terms on the right-hand side, $N_S = (L_i \Delta h_i)/(c_i h_i \Delta \bar{T})$, is a form of the Stefan number. Assuming $\Delta h = 0.5$m as a typical value for summer ablation and $\Delta \bar{T} = 10K$ to describe the seasonal variability of the column-averaged temperature, this implies that $N_S > 1$ as long as $h_i < 8m$, and hence latent heating dominates over sensible heating in this regime.

[28] Near the transition to seasonally ice-free conditions (edges of red shaded regions in Figure 1), the large Stefan number approximation employed here should hold in most parameter regimes because seasonal ice is relatively thin. When the ice is very thick (lowest areas of blue shaded regions in Figure 1), the approximation becomes less accurate.

### 2.4. Dimensionless Version of Model

[29] We are able to remove two parameters from the system (2)–(4) and (6) by scaling $E$ and $t$. Here we scale all parameters so that they are dimensionless, removing the annual period and the mean absorbed shortwave radiation

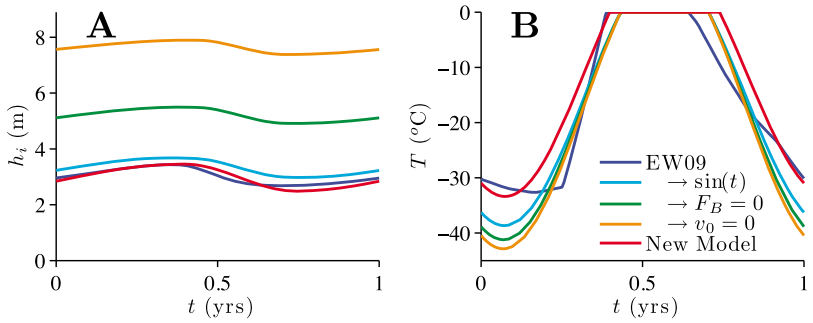


**Figure 3.** Derivation of the toy model used here from the model of EW09. (a) Seasonal cycle in ice thickness. (b) Seasonal cycle in ice surface temperature. Beginning with the model of EW09 (dark blue curves), the time-dependence of the forcing is approximated as sinusoidal (light blue), basal heating is set to zero (green), and ice export is turned off (orange). After re-adjusting the longwave forcing to offset these changes, we arrive at the toy model used in this study in the default parameter regime (red).

and clumping together parameters that do not appear independently.

[30] We scale time by the annual period ($P$) and scale enthalpy by the average shortwave radiation absorbed during one year ($\bar{\alpha} S_m P$). Fluxes are scaled by the mean absorbed shortwave radiation ($\bar{\alpha} S_m$). The thermodynamic scale thickness ($\zeta$) and smoothness of the albedo transition ($h_\alpha$) are both expressed in the same scaling as the dimensionless enthalpy. The albedo jump ($\Delta_\alpha$), while already being dimensionless, is scaled by twice the mean albedo. Finally, the temperature-dependent flux term is scaled with the ocean mixed layer heat capacity and the annual period. We represent dimensionless quantities by adding a tilde to the dimensional symbol. In terms of dimensionless quantities, equations (2)–(4) and (6) can be written as

$$\frac{d\tilde{E}}{d\tilde{t}} = \tilde{A} - \tilde{B}\tilde{T} + \tilde{F}_B, \tag{9}$$

$$\tilde{A} = \left(1 + \tilde{\Delta}_\alpha \tanh\frac{\tilde{E}}{\tilde{h}_\alpha}\right)\left(1 - \tilde{S}_a \cos 2\pi\tilde{t}\right) - \tilde{L}_m - \tilde{L}_a \cos 2\pi\left(\tilde{t} - \tilde{\phi}\right), \tag{10}$$

$$\tilde{T} = \begin{cases} \tilde{E} & \tilde{E} \geq 0 \quad \text{[open ocean]} \\ 0 & \tilde{E} < 0, \tilde{A} > 0 \quad \text{[sea ice, melting surface]} \\ \dfrac{\tilde{A}}{\tilde{B}}\left(1 - \dfrac{\tilde{\zeta}}{\tilde{E}}\right)^{-1} & \tilde{E} < 0, \tilde{A} < 0 \quad \text{[sea ice, frozen surface]} \end{cases}. \tag{11}$$

The values for each dimensionless parameter, as well as the dimensional definitions, are listed in Table 1.

### 2.5. Numerical Solutions

[31] Figure 4a shows simulations of a single year in the toy model starting from three different initial conditions. The black curve in Figure 4a ends at the same value of $\tilde{E}$ as it started from, and the green curves above and below it slightly converge on the black curve, indicating that the black curve is a stable steady state seasonal cycle solution of the toy model.

[32] In order to identify all stable and unstable solutions in a given parameter regime, we generate a one-year Poincaré map by beginning with a range of different initial conditions and numerically integrating them all forward for one year, as

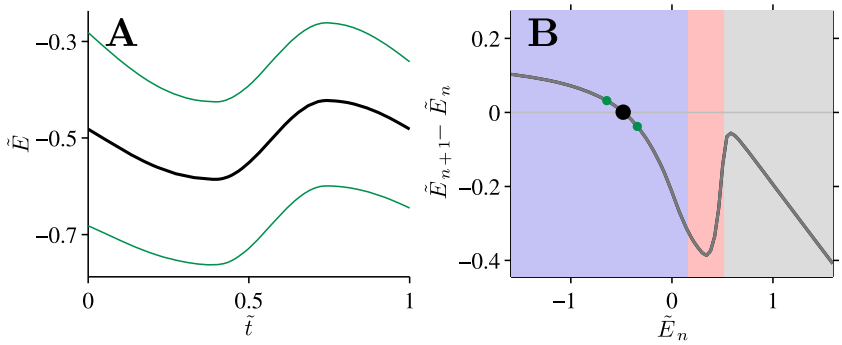


**Figure 4.** Poincaré map in the default parameter regime. (a) One-year trajectories for the steady state seasonal cycle solution (black) and years that begin with slightly warmer and colder initial conditions (green). (b) Poincaré map produced by integrating the toy model for one year from a range of different initial conditions. Black and green dots correspond to trajectories in Figure 4a. Similar to Figure 1, blue, red, and gray shading indicates one-year integrations that are continuously ice-covered, seasonally ice-free, and ice-free all year, respectively.

was done by EW09. Advantages of this method compared with the standard practice of integrating the model forward until it stops drifting are that this method identifies all stable and unstable solutions and that it is more efficient when forward integrations converge slowly.

[33] We define the model state at the winter solstice of year $n$ as $\tilde{E}_n \equiv \tilde{E}(\tilde{t} = n)$. The change in $\tilde{E}$ during the course of one year as a function of the initial condition is then defined as

$$F(\tilde{E}_n) \equiv \tilde{E}_{n+1} - \tilde{E}_n. \tag{12}$$

$F(\tilde{E}_n)$ is a version of the Poincaré map, which is a mapping from $\tilde{E}_n$ to $\tilde{E}_{n+1}$; note that we consider $\tilde{E}_{n+1} - \tilde{E}_n$ rather than $\tilde{E}_{n+1}$ in order to make the model behavior more clear in the figures, as was also done by *Abbot et al.* [2011].

[34] The Poincaré map reduces the seasonally varying ordinary differential equation (9)–(11) to a one-dimensional discrete map (12) that evolves $\tilde{E}$ from one winter solstice to the next. Fixed points of the Poincaré map ($\tilde{E}^*$) occur when $F(\tilde{E}^*) = 0$ and correspond to steady state seasonal cycle solutions of the model. Those with slope $F'(\tilde{E}^*) > 0$ are unstable and those with slope $-1 < F'(\tilde{E}^*) < 0$ are stable. Note that $-2 < F'(\tilde{E}^*) < -1$ corresponds to a stable oscillatory fixed point of the Poincaré map and $F'(\tilde{E}^*) < -2$ corresponds to an unstable oscillatory fixed point, but for all parameter regimes considered in this study $F'(\tilde{E}^*) > -1$. Small perturbations about a stable fixed point $\tilde{E}^*$ can be readily shown to exponentially decay with a timescale of

$$\tau = \frac{-P}{\log\left[1 + F'(\tilde{E}^*)\right]}, \tag{13}$$

which is related to the Lyapunov exponent for the stable attractor. Stable fixed points with a flatter slope $F'(\tilde{E}^*)$ have a slower decay timescale $\tau$ and a lower degree of stability. Saddle-node bifurcations occur when a stable fixed point merges with an unstable fixed point and disappears as the parameters are varied, at which point $F'(\tilde{E}^*) \to 0$ and $\tau \to \infty$. For further details see, e.g., *Strogatz* [1994, chapter 10].

[35] The Poincaré map in the default parameter regime is numerically generated for a range of initial conditions in Figure 4b. There is only one fixed point in this parameter regime (black circle in Figure 4b) and it is stable. Similar to Figure 1, blue shading indicates initial conditions with one-year integrations that are ice-covered all year, red shading indicates integrations that are seasonally ice-free, and gray shading indicates integrations that are ice-free all year. One-year integrations that begin with an ice-free initial condition ($\tilde{E}_n > 0$) but quickly cool and remain ice-covered for all $\tilde{t} > 0.25$ are considered ice-covered all year and shaded blue in Figure 4 because there is ice during the entire summer. The ice-albedo feedback is a destabilizing influence on seasonally ice-free one-year integrations, causing a positive slope in much of the red-shaded region. The associated bump on the right-hand edge this region implies the possibility of a pair of stable and unstable fixed points being created by a saddle-node bifurcation in response to warming, as will be discussed in section 3.

[36] Abrupt transitions associated with the temperature and albedo thresholds occur during the seasonal cycle in some parameter regimes, which can cause difficulties in one-year numerical integrations of the system (9)–(11). For each of the figures included in this study, the system was integrated separately with two different solvers: an explicit Runge–Kutta solver and an implicit variable order solver. When the solvers differ in terms of the number and type of solutions in a given parameter regime, the solution is chosen based on a visual inspection of the smoothness of the Poincaré map.

### 2.6. Ice-Free Model States

[37] Purely ice-free model states are approximately linear and can be readily solved analytically. Taking the annual mean of equations (9)–(11) in the regime $\tilde{E}/\tilde{h}_\alpha \gg 1$ leads to

$$\frac{d\langle\tilde{E}\rangle}{d\tilde{t}} = \frac{\langle\tilde{E}^*\rangle - \langle\tilde{E}\rangle}{\tilde{\tau}}, \tag{14}$$

which describes the annual-mean model state $\langle\tilde{E}\rangle$ evolving toward the fixed point $\langle\tilde{E}^*\rangle \equiv (1 + \tilde{\Delta}_\alpha - \tilde{L}_m + F_B)/\tilde{B}$ with an exponential decay timescale of $\tilde{\tau} \equiv 1/\tilde{B}$, which is the dimensionless version of the quantity given in equation (13), $\tilde{\tau} = \tau/P$. We integrate the system forward one year to find the Poincaré map,

$$F(\tilde{E}_n) = \left(\tilde{E}_n - \langle\tilde{E}^*\rangle + \delta_{\tilde{E}}\right)\left(e^{-\tilde{B}} - 1\right), \tag{15}$$

where the vertical offset $\delta_{\tilde{E}} \equiv [\tilde{S}_a\tilde{B}(1 + \tilde{\Delta}_\alpha) + \tilde{L}_a(\tilde{B}\cos 2\pi\tilde{\phi} - 2\pi \sin 2\pi\tilde{\phi})]/(\tilde{B}^2 + 4\pi^2)$ is due to the phase of the seasonal cycle at the reference time $\tilde{t} = 0$. Equation (15) describes the straight line in the gray region of Figure 4b.

## 3. Response to Warming

[38] The toy model is warmed by varying the annual-mean longwave forcing $\tilde{L}_m$, which is equivalent to the method used by EW09 and is intended to serve as an analogy for greenhouse-induced climate change. For each value of $\tilde{L}_m$ in Figure 5a, a Poincaré map is numerically generated. The thick curve indicates values of the fixed points of the Poincaré map ($\tilde{E}^*$), and the thin curves indicate the summer maximum and winter minimum values of $\tilde{E}$ during the one-year integration for each fixed point (i.e., the associated steady state seasonal cycle). As in Figure 1, solid black curves in Figure 5a indicate stable states, dashed orange curves indicate unstable states, values of $\tilde{E}^*$ with one-year integrations that are perennially ice-covered are shaded blue, values with seasonally ice-free conditions are shaded red, and values with conditions that are ice-free throughout the year are shaded gray. In other words, the shading in Figure 5a at the location of the thick curve (fixed point of Poincaré map) changes color whenever a thin curve directly above or below it (maximum or minimum value during the year) crosses $\tilde{E} = 0$.

[39] The left edge of Figure 5a ($\tilde{L}_m = 1.25$) corresponds to the default parameter regime. As the climate is warmed, the toy model initially makes a smooth transition to seasonally ice-free conditions, but a discontinuity in the stable solution occurs during the transition to annually ice-free conditions due to a pair of saddle-node bifurcations creating and then

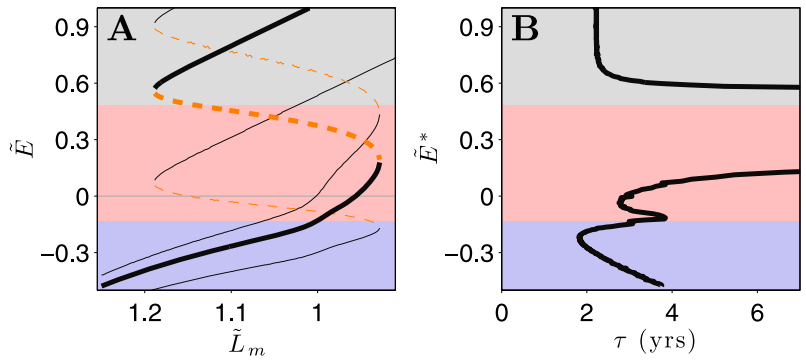


**Figure 5.** Bifurcation diagram and stability timescale with default parameters except $\tilde{L}_m$, which is varied. (a) Bifurcation diagram indicating stable fixed points (thick solid curves) and unstable fixed point (thick dashed curve), $\tilde{E}^*$, of the Poincaré map as the climate is warmed by scaling $\tilde{L}_m$. Thin curves indicate the summer maximum and winter minimum values of $\tilde{E}$ in the steady state seasonal cycle associated with each fixed point of the Poincaré map. Blue, red, and gray shading indicate steady state seasonal cycles which are perennially ice-covered, seasonally ice-free, and ice-free all year, respectively. (b) Decay timescale (horizontal axis) for perturbations about the stable fixed points, given by equation (13).

destroying an unstable fixed point. Hence the toy model simulates Scenario II in the default parameter regime, as in the results of EW09.

[40] The stability timescale from equation (13) is plotted in Figure 5b. Near the bottom of the figure, the ice becomes more stable (smaller $\tau$) as it thins, as expected from more efficient heat conduction through thinner ice (see section 2.2). The timescale increases as either bifurcation point is approached, with $\tau \rightarrow \infty$ at the actual bifurcation points and $\tau < 0$ (not shown) in the range of $\tilde{E}^*$ where the solution is unstable. For solutions that are annually ice-free with $\tilde{E}/\tilde{h}_\alpha \gg \tilde{h}_\alpha$ throughout the year, the response time assumes the constant value from equation (14) of $\tau = P/\tilde{B} = 2.2$ years.

[41] A striking behavior in Figure 5b is that the system becomes less stable (larger $\tau$) during the transition from perennial ice (blue shading) to seasonal ice (red shading). Although there is no bifurcation during the transition, this implies that Scenario IV may be possible in this toy model in a parameter regime that augments this decrease in stability. This slowing down as the system warms to a seasonally ice-free state is identified and analyzed by *Moon and Wettlaufer* [2011] in the EW09 model in its default parameter regime; note that in the EW09 model, which includes a representation of ice export as a stabilizing influence, the timescale is shorter than in the toy model used here.

[42] Indeed, when we vary the parameters in the toy model, we find that Scenario IV and each of the other scenarios can be simulated (Figure 6). Increasing the dependence of outgoing longwave radiation on surface temperature leads to Scenario I, Scenario II occurs in the default parameter regime, Scenario III occurs when the longwave seasonal cycle amplitude is reduced, and making the albedo transition more abrupt leads to Scenario IV. Note that the bifurcations do not occur at the exact transition to seasonally ice-free conditions due to the smoothing of the albedo transition ($\tilde{h}_\alpha$).

## 4. Mechanisms for Unstable Fixed Points

[43] Since each discontinuity in the black curves in Figure 6 is associated with the creation or annihilation of an unstable fixed point by a saddle-node bifurcation, we can analyze the threshold behavior by considering the factors controlling the presence of the unstable states.

### 4.1. Scenarios II and III

[44] The evolution of the toy model can be viewed in terms of three distinct feedbacks, which are illustrated in

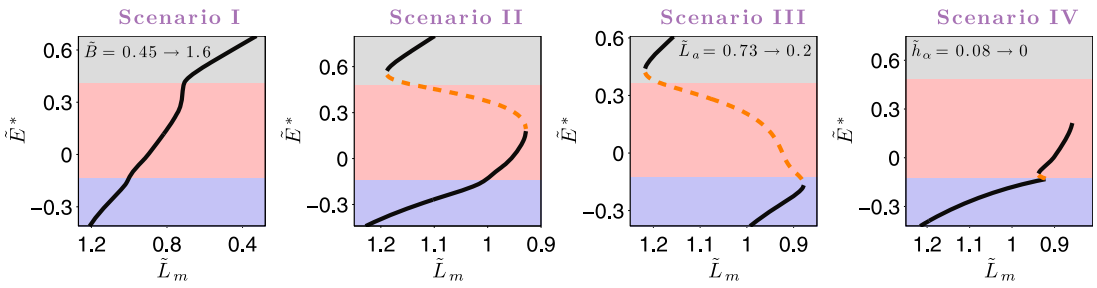


**Figure 6.** Bifurcation diagrams in four different parameter regimes. Thick solid and dashed curves and shading are as described in Figure 5a. By varying the parameters, the toy model is able to produce all four of the scenarios in Figure 1. Here $\tilde{B} = 1.6$ for Scenario I, $\tilde{L}_a = 0.2$ for Scenario III, $\tilde{h}_\alpha = 0$ for Scenario IV, $\tilde{L}_m$ is varied in all panels, and all other parameters are set at their default values.

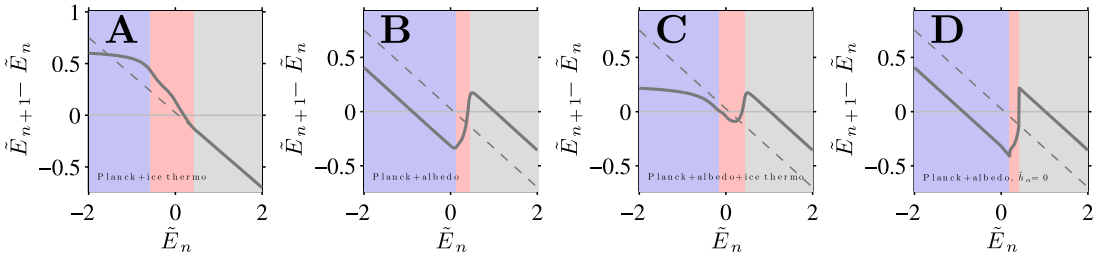


**Figure 7.** Poincaré maps illustrating specific feedbacks. (a) Planck feedback plus ice thermodynamic effects. (b) Planck feedback plus albedo feedback. (c) Full toy model including Planck feedback, albedo feedback, and ice thermodynamic effects. (d) Planck feedback plus albedo feedback with a sharpened albedo transition. The dashed line in each panel indicates the Poincaré map with the Planck feedback only. Shading is as described in Figure 4b, and $\tilde{L}_m = 1.0$ in all panels.

Figure 7. The first is the Planck feedback (warmer surface emits more radiation), which is a linear stabilizer governed primarily by the parameters $\tilde{B}$ and $\tilde{\zeta}$. The second is due to sea ice thermodynamic effects associated with heat conduction and phase change (thin ice grows faster than thick ice), which is a nonlinear stabilizer governed primarily by the parameter $\tilde{\zeta}$. The third is the surface albedo feedback ($\tilde{E} > 0$ warms more than $\tilde{E} < 0$), which is a nonlinear destabilizing influence governed primarily by the parameters $\tilde{\Delta}_\alpha$ and $\tilde{h}_\alpha$.

[45] The effect of the Planck feedback alone can be seen by considering equations (9) and (10) with $\tilde{\Delta}_\alpha = 0$ and equation (11) replaced by

$$\tilde{T} = \tilde{E}, \tag{16}$$

in which case the equations for an ice-free ocean are used even when $\tilde{E} < 0$ (cf. EW09). The system (9), (10), and (16) with $\tilde{\Delta}_\alpha = 0$ reduces to equation (14) for all $\tilde{E}$. The Poincaré map for this linear system, which is given by equation (15), is indicated by the straight dashed line in each panel of Figure 7.

[46] The addition of sea ice thermodynamic effects to this picture (solid curve in Figure 7a) is represented by replacing equation (16) with equation (11), i.e., using the toy model (9)–(11) with $\tilde{\Delta}_\alpha = 0$. Compared with the dashed line in Figure 7a, the solid curve has a steeper negative slope for values of $\tilde{E}_n$ corresponding to seasonal cycles with thin ice and a less negative steep slope for thick ice. This illustrates that sea ice thermodynamic effects cause increased stability for solutions with thin ice and decreased stability for solutions with thick ice, as discussed in section 2.2.

[47] The system with only albedo and Planck feedbacks (solid curve in Figure 7b) is represented by equations (9), (10), and (16) with all parameters including $\tilde{\Delta}_\alpha$ at their default values. In this regime, one-year integrations that are perennially ice-covered (blue shading) or perennially ice-free (gray shading) have the same slope as the dashed line, obeying equation (15) except that the sign of $\tilde{\Delta}_\alpha$ is switched when $\tilde{E}_n < 0$. The entire seasonally ice-free region (red shading) is unstable due to the influence of the albedo feedback (cf. Figure 2 of EW09).

[48] All three feedbacks are included in Figure 7c, which is generated using the toy model (9)–(11) with default parameter values. This Poincaré map can be approximately visualized as a linear superposition of the Planck feedback (dashed line in each panel of Figure 7), the addition of sea ice thermodynamic effects (difference between solid and dashed curves in Figure 7a), and the addition of the albedo feedback (difference between solid and dashed curves in Figure 7b). Compared with Figure 7b, in Figure 7c the left-hand side of the seasonally ice-free region is stabilized by sea ice thermodynamic effects, whereas the perennial ice region is less stable. This allows stable seasonally ice-free solutions to occur on the left-hand side of the red shaded region in Figure 7c, where the slope of the Poincaré map is negative. Unstable seasonally ice-free solutions still occur on the right-hand side of the red shaded region, where the Poincaré map has a positive slope. This instance of Scenario II is equivalent to that described by EW09.

[49] When the climate is warmed by decreasing $\tilde{L}_m$, the change in the Poincaré map approximately resembles a uniform vertical shift upward. Warming the climate in the default parameter regime causes an unstable fixed point to be created and then destroyed via saddle-node bifurcations (Figure 8a). Initially, the unstable fixed point is created along with a stable fixed point that is ice-free all year when the bump near the right-hand edge of the red-shaded region crosses $\tilde{E}_{n+1} - \tilde{E}_n = 0$ (lower dashed curve in Figure 8a). Further warming causes the unstable fixed point to migrate to the left in Figure 8a as the Poincaré map continues to shift upward (thick solid curve in Figure 8a). The unstable fixed point and the colder stable fixed point merge and disappear when the dip at the left-hand edge of the region of the Poincaré map with positive slope rises above $\tilde{E}_{n+1} - \tilde{E}_n = 0$ (upper dashed curve in Figure 8a).

[50] As will be discussed below in section 5, varying the toy model parameter values changes the size of the unstable region in Figure 7c, i.e., the range of initial conditions for which the Poincaré map has a positive slope. The toy model produces Scenario III if the unstable region is large and Scenario II if the unstable region is small.

[51] We close this section by considering the relevance of the unstable fixed point associated with Scenarios II and III in the toy model to more comprehensive representations of the climate system. The Planck feedback is believed to be the dominant feedback in the global climate system [e.g., *Soden and Held*, 2006]. The feedback associated with ice thermodynamic effects has been found to apply robustly both to submarine observations and to large-scale mean quantities in GCMs [*Bitz and Roe*, 2004]. The broad qualitative

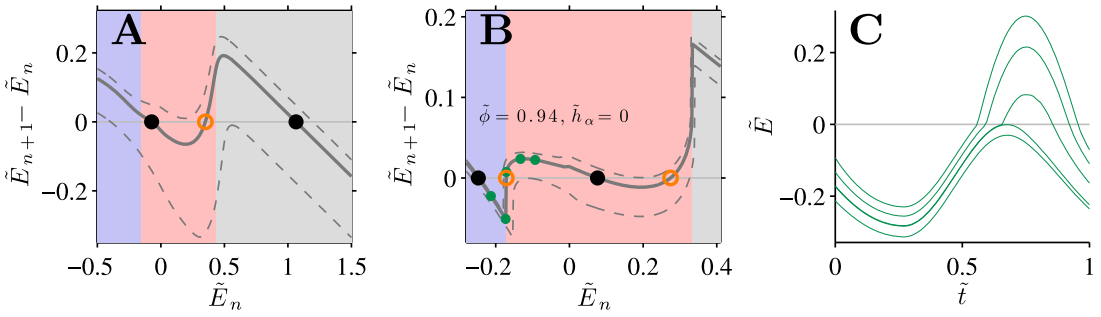


**Figure 8.** Poincaré maps and $\tilde{E}(\tilde{t})$ trajectories. (a) Poincaré map with default parameter values except $\tilde{L}_m = 0.98$ (solid curve). Stable and unstable fixed points are indicated by filled and open circles, respectively. Poincaré maps for a slightly warmer climate ($\tilde{L}_m = 0.92$) and slightly colder climate ($\tilde{L}_m = 1.20$) are included as dashed curves. Shading is as described in Figure 4b. (b) Same as Figure 8a but with $\tilde{\phi} = 0.94$, $\tilde{h}_\alpha = 0$, and $\tilde{L}_m = 1.04$; dashed curves have $\tilde{L}_m = 1.03$ and $\tilde{L}_m = 1.07$. Initial conditions slightly warmer and colder than the unstable fixed point on the left-hand side are indicated by small green circles. (c) One-year trajectories of $\tilde{E}$ associated with the green circles in Figure 8b.

features of the surface albedo feedback have been identified in satellite observations of the Arctic [*Perovich et al.*, 2007], as well as in global-mean quantities in GCMs [e.g., *Soden and Held*, 2006]. Hence the broad features of these three feedbacks may be expected to apply to basin-wide average quantities in the Arctic Ocean, and it is plausible that this unstable state exists in more physically complete spatially varying models and also in the real world. However, it is also plausible that the influence of spatial variability, motion, weather noise, and other physical processes would remove the unstable state.

### 4.2. Scenario IV

[52] The unstable fixed point associated with Scenario IV is caused by the crest of $\tilde{E}(\tilde{t})$ crossing zero when the albedo transition is sharp. The Poincaré map for Planck plus albedo feedbacks with $\tilde{h}_\alpha = 0$ is plotted in Figure 7d for comparison with the smoother albedo transition (using the default value of $\tilde{h}_\alpha = 0.08$) plotted in Figure 7b. At the left-hand edge of the red-shaded region in Figure 7d, where the initial conditions first become seasonally ice-free during the one-year integrations, there is a sharply positive slope that quickly levels off. Compared with Figure 7b, in Figure 7d the slope of the Poincaré map at the left-hand edge of the red-shaded region is considerably steeper, whereas the slope to the right of this narrow dip is considerably less steep. This can lead to a second unstable fixed point existing in a limited region of the parameter space.

[53] In Figure 8b (solid curve), an enlargement of the seasonally ice-free region of the Poincaré map is plotted including all three toy model feedbacks, using equations (9)–(11) with $\tilde{\phi}$, $\tilde{h}_\alpha$, and $\tilde{L}_m$ set to values near the bifurcation point associated with Scenario IV.

[54] The stable and unstable fixed points on the right-hand side of Figure 8b are the same as the stable and unstable seasonally ice-free fixed points in Figure 8a (see section 5.2), but there is an additional unstable fixed point in this parameter regime at the left-hand edge of the seasonally ice-free region of the Poincaré map, along with an additional stable fixed point in the blue shaded region.

[55] We consider one-year integrations starting from five different initial conditions, which are indicated by green dots in Figure 8b. The time series for each integration is plotted in Figure 8c. Starting from the coldest initial condition (lowest green curve in Figure 8c), increasing the initial value of $\tilde{E}$ (next higher green curve) causes the time series to just reach $\tilde{E} = 0$ at the warmest point of the year. When we further warm the initial condition by a very small amount, such that the increase in $\tilde{E}$ is almost indistinguishable during the first part of the year in Figure 8c, the flat crest of $\tilde{E}(\tilde{t})$ crosses above zero at the time of summer maximum. Due to the sharp albedo transition, this causes a large change in the amount of time that the surface is ice-free, and hence a large change in the annual absorbed solar radiation. Further incremental warming of the initial condition (two higher green curves in Figure 8c) causes only relatively small increases in the ice-free duration. The result is that the ice-albedo feedback is substantially more destabilizing near the boundary between blue and red regions of the Poincaré map in Figure 8b than in the rest of the red region, with an associated unstable fixed point.

[56] The dashed curves in Figure 8b, which represent slightly increased and decreased values of $\tilde{L}_m$, indicate that this unstable fixed point is created by a saddle-node bifurcation, as for the unstable fixed point discussed in section 4.1. Depending on the parameter regime, warming the system when both unstable fixed points exist can cause either of the unstable fixed points to be annihilated (see section 5.2). In parameter regimes such as that plotted in Figure 8b, as the climate is warmed from an ice-covered state (black circle in blue-shaded region), a series of two saddle-node bifurcations cause a stable seasonally ice-free fixed point to appear along with the unstable fixed point associated with Scenario IV and then to disappear along with the other unstable fixed point. This is represented in Figure 8b by a shift in the Poincaré map from the lower dashed curve to the solid curve and then to the upper dashed curve. The black circle in the blue-shaded region remains during these bifurcations, and hence the new seasonally ice-free stable fixed point is never visited during a warming scenario in the absence of an external forcing driving $\tilde{E}$ to the warmer fixed point. In other

parameter regimes, the left-hand region of the solid curve in Figure 8b with $\tilde{E}_{n+1} - E_n < 0$, rather than the right-hand region, rises above zero in response to warming. In these regimes, warming the climate leads to a point where the unstable fixed point merges with the perennial ice cover fixed point and the system abruptly transitions to seasonally ice-free conditions, demonstrating behavior consistent with Scenario IV. Further warming in these regimes causes an abrupt transition from seasonally ice-free conditions to annually ice-free conditions when the seasonally ice-free stable fixed point merges with the remaining unstable fixed point in a saddle-node bifurcation (see section 5.2).

[57] As discussed in section 5.2, the unstable fixed point associated with Scenario IV occurs when the albedo transition is sharp (varying $\tilde{h}_\alpha$) or when the seasonal cycle is shifted such that the crest of $\tilde{E}(\tilde{t})$ crosses zero near the summer solstice (varying $\tilde{\phi}$). In Figures 8b and 8c, we use a parameter regime that maximizes both of these factors.

[58] The unstable fixed point associated with Scenario IV depends crucially on the shape of the crest of $\tilde{E}(\tilde{t})$. Because not all points in a spatially varying representation of the climate have the same ice thickness, and hence they do not all reach zero at the same moment, the unstable fixed point associated with Scenario IV appears to be an artifact of a single-column representation. Specifically, this analysis implies that it would not occur in a representation that includes spatial variability in sea ice thickness. This unstable fixed point may coincide with the instability that is found by *Abbot et al.* [2011] to give rise to a tipping point during the transition from perennial to seasonal ice cover under some cloud feedback regimes.

## 5. Range of Possibilities

[59] In order to determine what controls which of the four scenarios in Figure 6 occurs in the toy model, we investigate the parameter dependence. The full range of solutions to the system (9)–(11) occupies a 9-dimensional parameter space (Table 1). Since the four bifurcation scenarios considered here (Figure 1) all occur during warming, we examine 2-dimensional planes of the parameter space by varying $\tilde{L}_m$ concurrently with each one of the other 8 parameters. Hence we address the question how the system would respond to forced warming if any one of the parameters were different from its default value.

[60] Figure 9 indicates what stable fixed points occur when the parameters are varied. Each point in each panel of Figure 9 represents a single point in the model parameter space. For each point, a Poincaré map is numerically generated for the range $-8 < \tilde{E}_n < 8$ and fixed points are identified. In some instances, a phase offset is used in the 1-year integrations when this is found to give a smoother numerical solution. Blue, red, and gray shading in Figure 9 represents regions with a stable fixed point corresponding to a steady state seasonal cycle with perennial ice, seasonally ice-free conditions, or annually ice-free conditions, respectively. Multiple states, and hence unstable fixed points, occur where shading of different colors overlaps. The bifurcation curves marking the edges of these parameter regions are drawn in black. The white regions in Figure 9 have ice thicker than the 50 m lower limit of the range of the Poincaré map. Note that all parameter regimes plotted in Figure 9 have no more than one stable fixed point of each of the three colored types.

[61] A green dot is included in each panel of Figure 9 to indicate the default parameter regime. Hence Figures 9a–9h all have identical behavior along the vertical line (not drawn) that passes through the green dot, which represents variations in $\tilde{L}_m$ with all other parameters at default values. The overlapping colors along this vertical line indicate Scenario II, as expected for the default parameter regime (section 3). This can be seen by comparison with Figure 6: in Scenario II, some values of $\tilde{L}_m$ have stable fixed points in both gray and blue regions and other values of $\tilde{L}_m$ have stable fixed points in both gray and red regions (with fixed points in gray regions occurring above the plotted range). Hence vertical lines in Figure 9 that have both gray overlapping with blue and gray overlapping with red indicate Scenario II. Vertical lines in Figure 9 with no overlapping colors indicate Scenario I, vertical lines with only gray and blue overlapping indicate Scenario III, and vertical lines with red and blue overlapping indicate Scenario IV.

[62] There is a single area in each panel of Figures 9a–9h that has gray overlapping red or blue. This implies that the 8 parameter planes plotted in Figures 9a–9h represent slices of a single continuous 9-dimensional hyper-volume of the parameter space in which this unstable fixed point occurs. Hence all instances of Scenario II and III in the toy model are expected to be due to a single physical mechanism, namely the mechanism discussed in section 4.1 above.

[63] Overlap between red and blue shading (indicating Scenario IV) occurs in only a small area of the parameter surfaces explored here, occurring when $\tilde{h}_\alpha < 0.01$ in Figure 9h and when $-0.14 < \tilde{\phi} < 0.01$ in Figure 9f (note that $\tilde{\phi}$ is defined modulo 1). The slices of parameter space plotted in Figure 9 do not allow us to distinguish whether this unstable fixed point in Figure 9h is connected to that in Figure 9f. In order to address this, two additional planes of the parameter space which connect the relevant regions of Figure 9f and Figure 9h are plotted in Figure 10. The first parameter plane (Figure 10a) connects the vertical line in Figure 9h ($\tilde{h}_\alpha = 0.001$, $\tilde{\phi} = 0.15$) to an intermediate parameter region ($\tilde{h}_\alpha = 0.001$, $\tilde{\phi} = 0.94$). The second parameter plane (Figure 10b) connects this intermediate region with the vertical line in Figure 9f ($\tilde{h}_\alpha = 0.08$, $\tilde{\phi} = 0.94$). The results plotted in Figure 10 indicate that the points where red and blue overlap in Figures 9h and 9f are indeed connected in the parameter space, and hence that they both represent the same unstable state which occurs in a single continuous hyper-volume of the parameter space and is expected to be governed by the single physical mechanism discussed in section 4.2 above. Figure 10 also implies that the detailed structure of the panels in Figure 9 and the widths of the unstable regions in Figure 6 depend on the default parameter values.

[64] In most regions of the parameter space plotted in Figures 9 and 10 where the unstable fixed point associated with Scenario IV occurs (red overlapping with blue), the unstable fixed point associated with Scenarios II and III also occurs (gray overlapping with red or blue); a small region of Figure 10b is the exception. Hence in these regions of the parameter space there are 3 stable fixed points and 2 unstable fixed points, and any of the 5 associated steady state

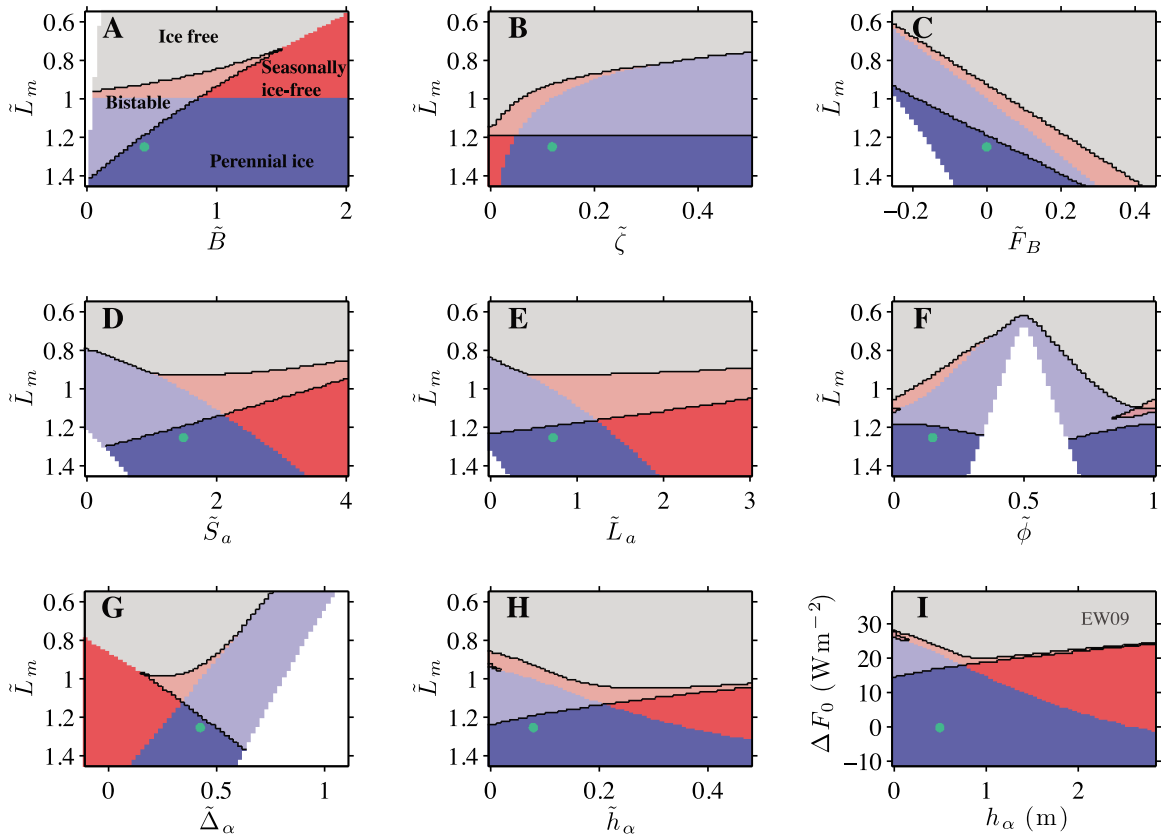


**Figure 9.** Classes of stable fixed points and bifurcation curves under varied parameters. For each point in each panel, a one-year Poincaré map is generated for the range $-8 < \tilde{E}_n < 8$ and the fixed points are identified. Stable fixed points representing perennial ice, seasonally ice-free conditions, and annually ice-free conditions are identified by blue, red, and gray shading, respectively. Regions with multiple stable fixed points are indicated by overlapping shades, and the bifurcation curves marking the edges of these regions are indicated by black curves. Dimensionless parameters in the vertical and horizontal axis labels in each panel are as defined in Table 1, except in Figure 9i where the results of the EW09 model are plotted using ranges of the EW09 dimensional parameters equivalent to the toy model dimensionless parameter ranges plotted in Figure 9h. Note that the upward direction on the vertical axis corresponds to warmer climates and lower values of $\tilde{L}_m$. White areas indicate points where the coldest initial condition leads to further cooling, implying ice thicker than the 50 m limit of the range considered here. The green dot in each panel indicates the default parameter regime. Each panel includes 100 equally spaced values of $\tilde{L}_m$ and 60 equally spaced values of a second model parameter.

seasonal cycle solutions are possible depending on the initial condition.

### 5.1. Scenarios I, II, and III

[65] Here we examine the occurrence of gray overlapping with red or blue in Figure 9, which determines whether Scenario I, II, or III occurs. In order to understand the physical mechanisms controlling the parameter dependencies in Figure 9, we also consider how the annual-mean model state depends on the parameter values (Figure 11).

#### 5.1.1. Size of Albedo Jump ($\tilde{\Delta}_\alpha$)

[66] The range of physical factors controlling the size of the unstable state associated with Scenarios II and III can be understood by primarily considering only Figures 9g and 11g. Decreasing the albedo jump ($\tilde{\Delta}_\alpha$) makes perennial ice solutions absorb more solar radiation and hence have thinner ice, and it makes annually ice-free solutions absorb less solar radiation and hence have colder ocean temperatures (Figure 11g). This is favorable to seasonally ice-free conditions because it enhances the thinning of the ice and the cooling of the ocean, promoting transitions between the two regimes (increased red area in Figure 9g). It is not conducive to multiple states and hence unstable fixed points because it is discourages the coexistence of ice-covered and ice-free solutions under the same forcing (decreased region of overlap in Figure 9g).

[67] Hence as the albedo jump ($\tilde{\Delta}_\alpha$) is decreased, the region of instability decreases, going from Scenario III (where there is no red region, and the system jumps from blue to gray, on the right-hand side of Figure 9g) to Scenario II (where there is a small instance of bistability over the transition from red to gray) to Scenario I (where the system transitions continuously from red to gray on the left-hand side of Figure 9g). Note that the albedo jump $\tilde{\Delta}_\alpha$ depends physically on many factors including snow cover

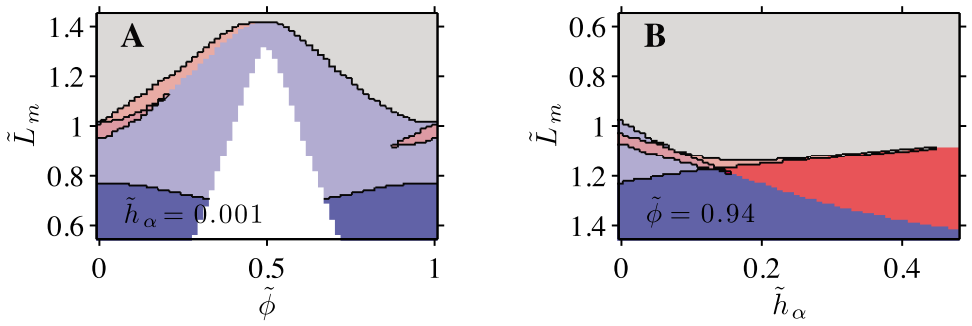


**Figure 10.** Planes of the parameter space connecting the regions where blue and red shading overlaps in Figures 9f and 9h. (a) Same as Figure 9f but with $\tilde{h}_\alpha = 0.001$. (b) Same as Figure 9h but with $\tilde{\phi} = 0.94$.

and the age of the ice, as well as clouds which influence the planetary albedo.

[68] Similar arguments can be applied to each of the other parameters: in all panels of Figures 9 and 11, parameter shifts that cause thinner perennial ice or colder ice-free ocean temperatures (lighter shades of red and blue in Figure 11) make the system more conducive to seasonally ice-free solutions (larger red region in Figure 9) and less conducive to instability (smaller overlap region in Figure 9).

#### 5.1.2. Smoothness of Albedo Jump ($\tilde{h}_\alpha$)

[69] Increasing the value of $\tilde{h}_\alpha$ reduces the difference in albedo between thin ice and open water near the melting point, and hence it is analogous to decreasing $\tilde{\Delta}_\alpha$. It leads to annual-mean values of $\tilde{E}$ that are nearer to zero (Figure 11h), but unlike a decrease in $\tilde{\Delta}_\alpha$, it has this effect only when $\tilde{E}$ is near zero. Nonetheless, because this is the range of $\tilde{E}$ that is relevant to the transition between ice and open water, increasing $\tilde{h}_\alpha$ leads to a larger region with stable seasonally ice-free solutions and a smaller region with bistability. The parameter $\tilde{h}_\alpha$ is meant to characterize both the dependence of albedo on the thickness of bare ice in a given location [e.g., *Weller*, 1972] and the influence of spatial variability on the relationship between the spatial-mean surface albedo and spatial-mean surface enthalpy.

#### 5.1.3. Temperature Dependence of Surface Flux ($\tilde{B}$) and Scale Thickness ($\tilde{\zeta}$)

[70] The Planck feedback is controlled by the dimensional parameter $B$, which is part of the dimensionless parameters $\tilde{B}$ and $\tilde{\zeta}$. Ice-free solutions are not influenced by $\tilde{\zeta}$ (upper region of Figures 9b and 11b), whereas ice-covered solutions

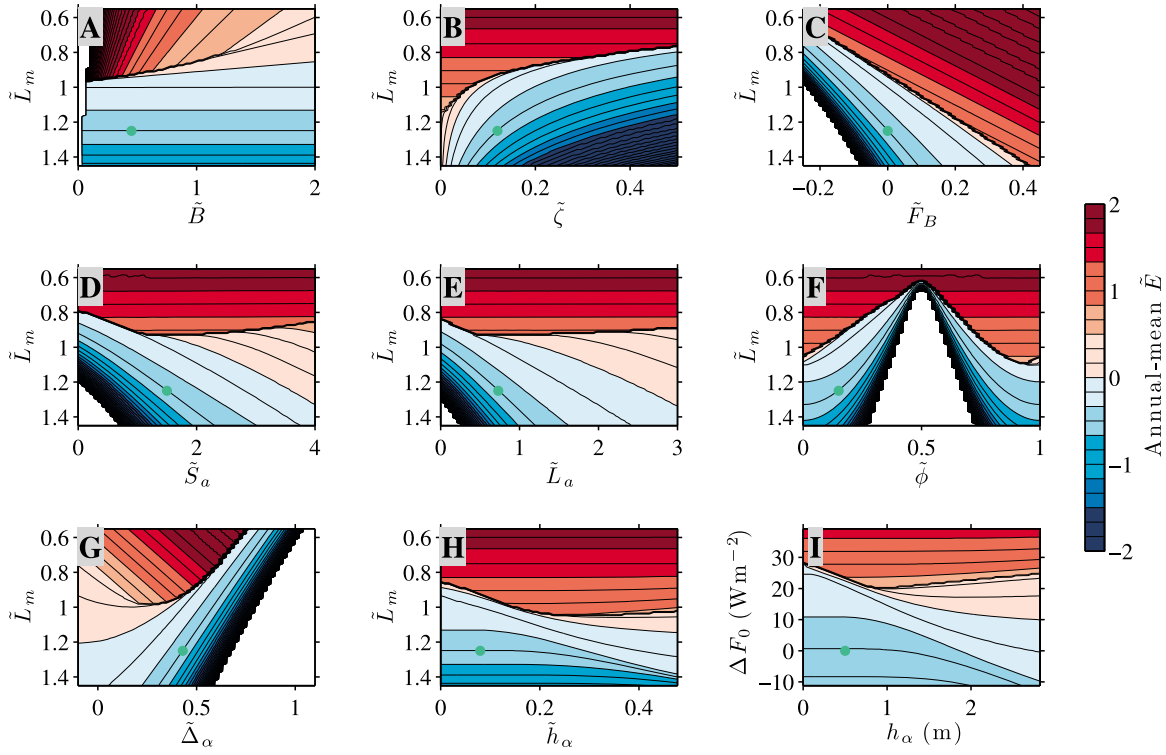


**Figure 11.** Annual-mean model state under varied parameters. The panels are as described in Figure 9, with the green dot indicating the default parameter regime. For each point in each panel, the annual-mean value of $\tilde{E}$ associated with the coldest stable fixed point is plotted.

are not influenced by $\tilde{B}$ because the system (9)–(11) does not depend on $\tilde{B}$ when $\tilde{E} < 0$ (lower region of Figures 9a and 11a).

[71] According to equation (14), the annual-mean value of $\tilde{E}$ for ice-free solutions is inversely proportional to $\tilde{B}$. Hence larger values of $\tilde{B}$ make the ice-free ocean temperature colder. This leads to a larger region with stable seasonally ice-free solutions and a smaller region with bistability. The dimensional parameter $B$ depends physically on the myriad factors which control the climate sensitivity, which is equal to $1/B$. The dimensionless parameter $\tilde{B}$ also depends on the ocean mixed layer depth, and hence the results in Figure 9a are consistent with the finding by *Björk and Söderkvist* [2002] that a shallow mixed layer promotes solutions with stable seasonal ice.

[72] For ice-covered solutions, $h_i/\zeta$ becomes larger when $\zeta$ is decreased and hence ice of thickness $h_i$ grows more slowly during winter (see section 2.2), leading to solutions with thinner ice (Figure 11b). Hence small values of $\tilde{\zeta}$ have an effect on the $\tilde{E} < 0$ region of Figure 11b analogous to the effect of large values of $\tilde{B}$ on the $\tilde{E} > 0$ region. Note that both of these scenarios are associated with an increase in the dimensional parameter $B$. In Figure 9b, smaller values of $\tilde{\zeta}$ are associated with larger regions with stable seasonally ice-free solutions and smaller regions with bistability. The parameter $\tilde{\zeta}$ is proportional to the sea ice thermal conductivity ($k_i$), the latent heat of fusion $L_i$, and the climate sensitivity ($1/B$). The presence of leads makes the ice more conductive, increasing $\tilde{\zeta}$ and thereby leading to thicker ice. The presence of snow decreases thermal conductivity and hence $\tilde{\zeta}$, leading to thinner ice [cf. *Notz*, 2009], although the additional degree of freedom associated with varying snow thickness could plausibly cause a substantial change in the bifurcation structure.

#### 5.1.4. Basal Heat Flux ($\tilde{F}_B$)

[73] An increase in $\tilde{F}_B$ when $\tilde{E} > 0$ has the same effect as an equal decrease in $\tilde{L}_m$, since in this regime $\tilde{F}_B - \tilde{L}_m$ may be written as a single parameter in equation (14). However, sea ice is more sensitive to heating from below ($\tilde{F}_B$) than from above ($\tilde{L}_m$). This is because heating the surface (increasing $\tilde{A}$) leads to warmer wintertime surface temperatures and hence some of the heating perturbation is lost to surface radiation ($\tilde{B}\tilde{T}$). Heating the base (increasing $\tilde{F}_B$), by contrast, does not directly influence the surface temperature, so all of the heating perturbation goes into inhibiting ice growth in equation (9). The influence of perturbations to both the surface and basal fluxes ($\tilde{A} \rightarrow \tilde{A} + \delta\tilde{A}$, $\tilde{F}_B \rightarrow \tilde{F}_B + \delta\tilde{F}_B$) on the evolution of $\tilde{E}$ during ice-covered winter ($\tilde{E} < 0$, $\tilde{A} < 0$) can be written, from equations (9) and (11), as

$$\frac{d\delta\tilde{E}}{d\tilde{t}} = \delta\tilde{A}\left(1 - \frac{\tilde{E}}{\tilde{\zeta}}\right)^{-1} + \delta F_B. \tag{17}$$

This illustrates the greater efficacy of basal heating compared with surface heating. During summer ($\tilde{A} > 0$), however, the surface temperature is fixed at the melting point, and heating from above and below both have an equal effect on the amount of summer sea ice melt in equations (9)–(11). Hence the annual effect of an increase in $\tilde{F}_B$ is to thin the ice more than ice-free solutions are warmed (Figure 11c), which leads to a regime more conducive to stable seasonally ice-free conditions and less conducive to bistability (Figure 9c). The rate of basal heating ($\tilde{F}_B$) is associated with heat flux convergence driven by ocean currents and the stability of the upper ocean, as well as factors including the velocity of upper ocean currents relative to the sea ice.

#### 5.1.5. Seasonal Amplitude ($\tilde{S}_a$ and $\tilde{L}_a$)

[74] Figures 11d and 11e illustrate nonlinear rectification of the seasonal cycle when sea ice is present. An increase in $\tilde{S}_a$ or $\tilde{L}_a$ leads to both more summer heating and more winter cooling. During summer, however, the Planck feedback is inactive because the temperature in equation (11) is fixed at the melting point. Hence all of the additional summer heating leads to increased ice ablation ($d\tilde{E}/d\tilde{t}$), whereas the additional winter cooling is divided between increased ice growth and decreased surface longwave radiation associated with the Planck feedback ($\tilde{B}\tilde{T}$), leading to annual-mean thinning. This may help explain why sea ice thickness in the single-column model of *Bitz et al.* [1996] was more sensitive to forcing in summer than in winter. A further implication is that this mechanism governing the thermodynamic response of sea ice to the amplitude of the seasonal cycle of the forcing may help explain the nonlinear response of sea ice in climate models to orbital precession, which is typically attributed instead to the surface albedo feedback [*Jackson and Broccoli*, 2003; *Tuenter et al.*, 2005].

[75] When the system is ice-free, by contrast, the equations are linear and hence the annual-mean value of $\tilde{E}$ does not depend on $\tilde{S}_a$ or $\tilde{L}_a$ (Figures 11d and 11e). Thinner ice and unchanged ocean temperatures lead to a larger parameter region with stable seasonally ice-free conditions and a smaller parameter region with bistability, as discussed above. In addition, a simple linear system such as the toy model with only the Planck feedback (dashed line in the panels of Figure 7) would also have a larger region with seasonally ice-free solutions when $\tilde{S}_a$ or $\tilde{L}_a$ is increased because the seasonal cycle in $\tilde{E}$ would be larger and hence would cross $\tilde{E} = 0$ in a larger range of climates.

[76] A number of previous studies have identified multiple sea ice states in annual-mean representations of the climate. *Thorndike* [1999] found multiple states in a minimalistic annual-mean model of two interacting columns, and *Gildor and Tziperman* [2001] and *Sayag et al.* [2004] found multiple sea ice states in a box model with several and then many grid points in the meridional direction. Simulations with an atmospheric GCM with annual-mean forcing above a thermodynamic ocean mixed layer with sea ice were also suggested to demonstrate multiple states [*Langen and Alexeev*, 2004], although it should be noted that the GCM results (their Figure 2) appear to possibly violate the "slope-stability theorem" for multiple sea ice states [*Cahalan and North*, 1979], and further inquiry may be merited. Figures 9d and 9e illustrate that, at least in the toy model used here, multiple states occur over a larger range of parameters when the seasonal cycle amplitude is smaller, and hence multiple sea ice states may be considerably more

prone to occur in annual-mean representations of climate than in more realistic seasonally varying representations.

#### 5.1.6. Seasonal Phase ($\tilde{\phi}$)

[77] The phase shift between the shortwave and longwave forcing components is varied in Figures 9f and 11f. When $\tilde{\phi}$ is decreased to 0 from the default value of 0.15, the amplitude of the total seasonal forcing, which is a superposition of shortwave and longwave components, increases. The effect of this is to increase the range of values of $\tilde{L}_m$ with stable seasonally ice-free solutions and to decrease the range with multiple states, analogous to increasing $\tilde{S}_a$ or $\tilde{L}_a$. When $\tilde{\phi}$ is increased to 0.5, the two components of the forcing are exactly out of phase with each other, leading to a minimum amplitude of variability in the forcing. If $\tilde{L}_m \geq (1 - \tilde{\Delta}_\alpha)(1 + \tilde{S}_a) - \tilde{L}_a = 0.70$, $\tilde{A}$ remains negative throughout the year, causing there to be no ice ablation, and hence the ice thickness grows without bound. The parameters $\tilde{S}_a$, $\tilde{L}_a$, and $\tilde{\phi}$ are influenced by factors including latitude, cloud feedbacks, water vapor, and meridional atmospheric energy transport.

### 5.2. Scenario IV

[78] The unstable fixed point associated with Scenario IV requires a strong destabilizing surface albedo feedback on the left edge of the seasonally ice-free region of the Poincaré map (positive slope in Figures 7d and 8b). This is influenced primarily by the phase lag between shortwave and longwave forcing ($\tilde{\phi}$) and the smoothness of the albedo transition ($\tilde{h}_\alpha$).

[79] The phase lag (Figure 9f) influences the strength of the shortwave forcing during the ice-free portion of the year. In the default parameter regime, the model state $\tilde{E}$ lags behind the shortwave forcing. When the system is warmed such that a transition to seasonally ice-free conditions occurs, the surface albedo changes during autumn, when solar radiation is weak, and there is only a modest change in surface forcing. Shifting the longwave forcing to an earlier phase causes the seasonal cycle in $\tilde{E}$ to be earlier, thereby causing the change in surface albedo associated with the loss of the summer minimum ice cover to occur at a time nearer the summer solstice (see Figure 8c). This causes a larger destabilizing albedo feedback associated with the initial transition from perennial to seasonal ice conditions.

[80] A small value of $\tilde{h}_\alpha$ sharpens the albedo feedback and thereby promotes instability (Figure 9h). Hence either a sharp albedo transition or an early seasonal cycle in $\tilde{E}(\tilde{t})$ promote the occurrence of Scenario IV.

### 5.3. Comparison With EW09

[81] The parameter sensitivity in the EW09 model is included in Figures 9 and 11 for comparison. The behavior of the toy model presented here is qualitatively equivalent to the EW09 model when the albedo transition smoothness and surface heating are varied (compare Figures 9h and 11h with Figures 9i and 11i), although quantitative differences exist.

[82] The presence of the unstable state associated with Scenario IV, which occurs near the left edge of Figure 9i, is lacking from Figure S4 of the online supplement to EW09 because these narrowly separated solutions were not picked up within the precision of the numerical solver used in EW09 in this small area of the parameter space. We note that this does not affect the central message of EW09. In this study, we have addressed this by using an implicit variable order solver in addition to a Runge–Kutta solver.

## 6. Discussion and Conclusions

[83] In summary, previous studies using single-column models and GCMs have produced the range of results described by Scenarios I-IV in Figure 1. We used a skeletal toy model to show that all of these scenarios are possible when the parameters are varied broadly as an analogy to varying the physical processes represented in the model. We found that depending on the parameter regime, bistability can occur in the large range described by Scenario III (as in the results of *Thorndike* [1992] and *Muller-Stoffels and Wackerbauer* [2011]), in the smaller range described by Scenario II (as in the results of *Winton* [2006, 2008], *Eisenman and Wettlaufer* [2009], and *Björk and Söderkvist* [2002]), or not at all following Scenario I (as in the results of *Winton* [2006, 2008] and *Armour et al.* [2011]). Parameter shifts that make ice thinner or ocean temperatures colder under a given climate forcing were shown to make the range of climates with bistability smaller and the range with seasonal ice larger, thereby determining whether Scenario I, II, or III occurs. We argued that Scenario IV (as in the results of *Abbot et al.* [2011], *Merryfield et al.* [2008], and *Flato and Brown* [1996]) occurs as an artifact of the single-column representation. The aim of this study was to build understanding of the fundamental processes governing the bifurcation structure of sea ice loss in the absence of spatial variability and motion.

[84] Although many aspects of the toy model used in this study are analogous to a column in a GCM, it is possible that sea ice threshold behavior would occur in GCMs due to the myriad other processes represented in GCMs that are not included in the toy model. For example, in the framework of this toy model, dynamic ice motion is expected to make ice thinner in cold climates by exporting ice from the polar region while leaving ocean temperatures in warm ice-free climates unaffected, thereby making the system more prone to stable seasonally ice-free conditions and less prone to bistability. However, the additional degrees of freedom associated with sea ice motion are not represented in the framework of this toy model. *Hibler et al.* [2006] found that a gridded model of sea ice circulation in the Arctic basin with narrow outlet passages under perpetual winter forcing produces multiple flow states. One stable state has thin ice and rapid ice export and the other stable state has an arch of nearly stationary thick ice blocking outflow through the passages. Hence the complex effects of sea ice motion, which are not included in the toy model used here, could plausibly play an important role in determining the bifurcation structure of sea ice retreat in GCMs.

[85] Nonetheless, the results of this study provide a framework for speculation about mechanisms underlying GCM simulation results. *Winton* [2006] found evidence that one GCM (MPI ECHAM5) simulated results consistent with Scenario II whereas another GCM (NCAR CCSM3) simulated results consistent with Scenario I. A separate study with CCSM3 yielded consistent results [*Armour et al.*, 2011], but the key difference between the two GCMs has

remained elusive. We can crudely consider each GCM as a collection of single columns in a specific parameter regime with variations in $\tilde{L}_m$ providing an analogy to both latitude and greenhouse forcing. The results presented here suggest that because CCSM3 is less prone to bistability than ECHAM5, it should be described by a toy model parameter regime that has thinner ice and colder ocean temperatures, and hence it should allow a stable seasonal sea ice cover in a wider range of values of $\tilde{L}_m$. Indeed, comparing the simulated mean seasonal cycles of Northern Hemisphere sea ice area in the two GCMs under forcing representing years 1900–2000 (using data from *Eisenman et al.* [2011]), we find that the amplitude is 40% larger in CCSM3. In other words, CCSM3 has 40% more area with a seasonal sea ice cover than ECHAM5 during the simulated 20th century, implying that CCSM3 is considerably more favorable to seasonal ice. This implies that if we only had the 20th century simulation results from the two GCMs, based on the results presented in this study we would predict that ECHAM5 is more prone to bistability, and hence more likely to simulate Scenario II rather than Scenario I in response to extreme warming, than CCSM3. This may help shed light on the differences between the two models that are responsible for their differing projections of sea ice stability in a warming world, thereby constraining which is more realistic. In particular, although the application of this toy model to the interpretation of GCMs must be treated cautiously, the results presented here suggest that the differing projections may be due to processes or parameter values that cause ECHAM5 to simulate thicker ice or warmer ice-free sea surface temperatures than CCSM3.

[86] **Acknowledgments.** I thank J. S. Wettlaufer, K. C. Armour, and D. S. Abbot for helpful comments on the manuscript. This work was supported by a NOAA Climate and Global Change Postdoctoral Fellowship administered by the University Corporation for Atmospheric Research, the Davidow Discovery Fund, and NSF grant ARC-1107795.

## References

Abbot, D. S., M. Silber, and R. T. Pierrehumbert (2011), Bifurcations leading to summer Arctic sea ice loss, *J. Geophys. Res.*, *116*, D19120, doi:10.1029/2011JD015653.

Armour, K. C., I. Eisenman, E. Blanchard-Wrigglesworth, K. E. McCusker, and C. M. Bitz (2011), The reversibility of sea ice loss in a state-of-the-art climate model, *Geophys. Res. Lett.*, *38*, L16705, doi:10.1029/2011GL048739.

Bitz, C. M., and G. H. Roe (2004), A mechanism for the high rate of sea ice thinning in the Arctic Ocean, *J. Clim.*, *17*(18), 3623–3632.

Bitz, C. M., D. S. Battisti, R. E. Moritz, and J. A. Beesley (1996), Low-frequency variability in the Arctic atmosphere, sea ice, and upper-ocean climate system, *J. Clim.*, *9*(2), 394–408.

Björk, G., and J. Söderkvist (2002), Dependence of the Arctic Ocean ice thickness distribution on the poleward energy flux in the atmosphere, *J. Geophys. Res.*, *107*(C10), 3173, doi:10.1029/2000JC000723.

Budyko, M. I. (1969), The effect of solar radiation variations on the climate of the Earth, *Tellus*, *21*, 611–619.

Cahalan, R. F., and G. R. North (1979), Stability theorem for energy-balance climate models, *J. Atmos. Sci.*, *36*(7), 1178–1188, doi:10.1175/1520-0469(1979)036<1178:ASTFEB>2.0.CO;2.

Eisenman, I. (2007), Arctic catastrophes in an idealized sea ice model, in *2006 Program of Studies: Ice (Geophysical Fluid Dynamics Program)*, *Tech. Rep. 2007–02*, pp. 133–161, Woods Hole Oceanogr. Inst., Woods Hole, Mass. [Available at http://www.whoi.edu/page.do?pid=12938.]

Eisenman, I., and J. S. Wettlaufer (2009), Nonlinear threshold behavior during the loss of Arctic sea ice, *Proc. Natl. Acad. Sci. U.S.A.*, *106*(1), 28–32, doi:10.1073/pnas.0806887106.

Eisenman, I., T. Schneider, D. Battisti, and C. Bitz (2011), Consistent changes in the sea ice seasonal cycle in response to global warming, *J. Clim.*, *24*, 5325–5335, doi:10.1175/2011JCLI4051.1.

Ferreira, D., J. Marshall, and B. Rose (2011), Climate determinism revisited: Multiple equilibria in a complex climate model, *J. Clim.*, *24*(4), 992–1012, doi:10.1175/2010JCLI3580.1.

Flato, G. M., and R. D. Brown (1996), Variability and climate sensitivity of landfast Arctic sea ice, *J. Geophys. Res.*, *101*(C11), 25,767–25,777.

Gildor, H., and E. Tziperman (2001), A sea-ice climate-switch mechanism for the 100 kyr glacial cycles, *J. Geophys. Res.*, *106*(C5), 9117–9133.

Hibler, W. D., J. K. Hutchings, and C. F. Ip (2006), Sea-ice arching and multiple flow states of Arctic pack ice, *Ann. Glaciol.*, *44*, 339–344, doi:10.3189/172756406781811448.

Holland, M. M., C. M. Bitz, and B. Tremblay (2006), Future abrupt reductions in the summer Arctic sea ice, *Geophys. Res. Lett.*, *33*, L23503, doi:10.1029/2006GL028024.

Holland, M., C. Bitz, L.-B. Tremblay, and D. Bailey (2008), The role of natural versus forced change in future rapid summer Arctic ice loss, in *Arctic Sea Ice Decline: Observations, Projections, Mechanisms, and Implications*, *Geophys. Monogr. Ser.*, vol. 180, edited by E. DeWeaver, C. Bitz, and B. Tremblay, pp. 113–150, AGU, Washington, D. C.

Jackson, C. S., and A. J. Broccoli (2003), Orbital forcing of Arctic climate: Mechanisms of climate response and implications for continental glaciation, *Clim. Dyn.*, *21*(7–8), 539–557.

Langen, P. L., and V. A. Alexeev (2004), Multiple equilibria and asymmetric climates in the CCM3 coupled to an oceanic mixed layer with thermodynamic sea ice, *Geophys. Res. Lett.*, *31*, L04201, doi:10.1029/2003GL019039.

Lenton, T. M., H. Held, E. Kriegler, J. W. Hall, W. Lucht, S. Rahmstorf, and H. J. Schellnhuber (2008), Tipping elements in the Earth's climate system, *Proc. Natl. Acad. Sci. U. S. A.*, *105*(6), 1786–1793, doi:10.1073/pnas.0705414105.

Maykut, G. A., and N. Untersteiner (1971), Some results from a time-dependent thermodynamic model of sea ice, *J. Geophys. Res.*, *76*, 1550–1575.

Merryfield, W., M. Holland, and A. Monahan (2008), Multiple equilibria and abrupt transitions in Arctic summer sea ice extent, in *Arctic Sea Ice Decline: Observations, Projections, Mechanisms, and Implications*, *Geophys. Monogr. Ser.*, vol. 180, edited by E. DeWeaver, C. Bitz, and B. Tremblay, pp. 151–174, AGU, Washington, D. C.

Moon, W., and J. S. Wettlaufer (2011), A low-order theory of Arctic sea ice stability, *Europhys. Lett.*, *96*, 39001, doi:10.1209/0295-5075/96/39001.

Muller-Stoffels, M., and R. Wackerbauer (2011), Regular network model for the sea ice-albedo feedback in the arctic, *Chaos*, *21*(1), 013111, doi:10.1063/1.3555835.

North, G. R. (1990), Multiple solutions in energy-balance climate models, *Global Planet. Change*, *82*(3–4), 225–235.

Notz, D. (2009), The future of ice sheets and sea ice: Between reversible retreat and unstoppable loss, *Proc. Natl. Acad. Sci. U. S. A.*, *106*(49), 20,590–20,595, doi:10.1073/pnas.0902356106.

Perovich, D. K., B. Light, H. Eicken, K. F. Jones, K. Runciman, and S. V. Nghiem (2007), Increasing solar heating of the Arctic Ocean and adjacent seas, 1979–2005: Attribution and role in the ice-albedo feedback, *Geophys. Res. Lett.*, *34*, L19505, doi:10.1029/2007GL031480.

Ridley, J., J. Lowe, and D. Simonin, (2008), The demise of Arctic sea ice during stabilisation at high greenhouse gas concentrations, *Clim. Dyn.*, *30*(4), 333–341, doi:10.1007/s00382-007-0291-4.

Sayag, R., E. Tziperman, and M. Ghil (2004), Rapid switch-like sea ice growth and land ice-sea ice hysteresis, *Paleoceanography*, *19*, PA1021, doi:10.1029/2003PA000946.

Schroeder, D., and W. M. Connolley (2007), Impact of instantaneous sea ice removal in a coupled general circulation model, *Geophys. Res. Lett.*, *34*, L14502, doi:10.1029/2007GL030253.

Sellers, W. D. (1969), A global climate model based on the energy balance of the earth-atmosphere system, *J. Appl. Meteorol.*, *8*, 392–400.

Semtner, A. J. (1976), Model for thermodynamic growth of sea ice in numerical investigations of climate, *J. Phys. Oceanogr.*, *6*(3), 379–389.

Serreze, M. (2011), Rethinking the sea-ice tipping point, *Nature*, *471*, 47–48.

Soden, B. J., and I. M. Held (2006), An assessment of climate feedbacks in coupled ocean–atmosphere models, *J. Clim.*, *19*(14), 3354–3360.

Strogatz, S. H. (1994), *Nonlinear Dynamics and Chaos*, Perseus, Jackson, Tenn.

Thorndike, A. S. (1992), A toy model linking atmospheric thermal radiation and sea ice growth, *J. Geophys. Res.*, *97*, 9401–9410.

Thorndike, A. (1999), A minimal model of sea ice and climate, in *Ice Physics and the Natural Environment*, edited by J. S. Wettlaufer, J. G. Dash, and N. Untersteiner, pp. 169–183, Springer, New York.

Tietsche, S., D. Notz, J. H. Jungclaus, and J. Marotzke (2011), Recovery mechanisms of Arctic summer sea ice, *Geophys. Res. Lett.*, *38*, L02707, doi:10.1029/2010GL045698.

Tuenter, E., S. L. Weber, F. J. Hilgen, and L. J. Lourens (2005), Sea-ice feedbacks on the climatic response to precession and obliquity forcing, *Geophys. Res. Lett.*, *32*(24), L24704, doi:10.1029/2005GL024122.

Weller, G. (1972), Radiation flux investigation, *AIDJEX Bull.*, *14*, 28–30.

Winton, M. (2006), Does the Arctic sea ice have a tipping point?, *Geophys. Res. Lett.*, *33*, L23504, doi:10.1029/2006GL028017.

Winton, M. (2008), Sea ice-albedo feedback and nonlinear Arctic climate change, in *Arctic Sea Ice Decline: Observations, Projections, Mechanisms, and Implications*, *Geophys. Monogr. Ser.*, vol. 180, edited by E. DeWeaver, C. Bitz, and B. Tremblay, pp. 111–131, AGU, Washington, D. C.

I. Eisenman, Geological and Planetary Sciences, California Institute of Technology, 1200 California Blvd., Pasadena, CA 91125, USA. (ian@gps.caltech.edu)